


Article

Polymetallic Sulfide–Quartz Vein System in the Koudiat Aïcha Massive Sulfide Deposit, Jebilet Massif, Morocco: Microanalytical and Fluid Inclusion Approaches

Samira Essarraj ^{1,*}, Basem Zoheir ^{2,3}, Matthew Steele-MacInnis ⁴, Matthias Frische ⁵ , Abdelali Khalifa ⁶ and Abdelmalek Ouadjou ⁶

¹ Department of Earth Sciences, L3G, Faculty of Sciences and Technology, Cadi Ayyad University, Marrakesh 40000, Morocco

² Department of Geology, Faculty of Science, Benha University, Benha 13518, Egypt

³ Institut für Geowissenschaften, Universität Kiel, 24118 Kiel, Germany

⁴ Department of Earth & Atmospheric Sciences, 1-26 Earth Sciences Building, University of Alberta, Edmonton, AB T6G 2E3, Canada

⁵ GEOMAR Helmholtz Centre for Ocean Research Kiel, Wischhofstr. 1-3, 24148 Kiel, Germany

⁶ MANAGEM Group, Twin Center Tour A, 191, bd Mohamed Zerkoutouni, Angle bd. Massira Alkhadra, Casablanca 20100, Morocco

* Correspondence: s.essarraj@uca.ac.ma



Citation: Essarraj, S.; Zoheir, B.; Steele-MacInnis, M.; Frische, M.; Khalifa, A.; Ouadjou, A. Polymetallic Sulfide–Quartz Vein System in the Koudiat Aïcha Massive Sulfide Deposit, Jebilet Massif, Morocco: Microanalytical and Fluid Inclusion Approaches. *Minerals* **2022**, *12*, 1396. <https://doi.org/10.3390/min12111396>

Academic Editor: Georgy Cherkashov

Received: 13 October 2022

Accepted: 26 October 2022

Published: 31 October 2022

Publisher's Note: MDPI stays neutral with regard to jurisdictional claims in published maps and institutional affiliations.



Copyright: © 2022 by the authors. Licensee MDPI, Basel, Switzerland. This article is an open access article distributed under the terms and conditions of the Creative Commons Attribution (CC BY) license (<https://creativecommons.org/licenses/by/4.0/>).

Abstract: The Koudiat Aïcha Zn–Cu–Pb deposit (3–Mt ore @ 3 wt.% Zn, 1 wt.% Pb, 0.6 wt.% Cu) in the Jebilet massif (Morocco) comprises stratabound lenticular orebodies and crosscutting sulfide-bearing quartz ± carbonate veins in the lower Carboniferous Sarhlef volcano sedimentary succession. The veins are characterized by abundant pyrrhotite, sphalerite, subordinate chalcopyrite and galena and rare Ag and Au minerals. The stratabound massive sulfide ores are attributed to a “VMS” type, whereas the origin of the sulfide–quartz ± carbonate veins remains poorly understood. New mineralogical and microanalytical data (SEM, EPMA and LA-ICP-MS) combined with fluid inclusion results point to two-stage vein formation. The early stage involved C–H–O–N Variscan metamorphic fluids which percolated through fractures and shear zones and deposited pyrite at >400 °C, followed by the formation of pyrrhotite and sphalerite (300 ± 20 °C) in quartz veins and in banded and breccia ores. The pyrrhotite–sphalerite mineralization was overprinted by aqueous brines (34 to 38 wt% eq. NaCl + CaCl₂) that precipitated carbonate and Cu–Pb sulfides (±Ag–Au) at ~180–210 °C through mixing with low-salinity fluids during tectonic reworking of early-formed structures and in late extension fractures. The latter ore fluids were similar to widespread post-Variscan evaporitic brines that circulated in the Central Jebilet. Overlapping or successive pulses of different ore fluids, i.e., metamorphic fluids and basinal brines, led to metal enrichment in the quartz–carbonate veins compared to the massive sulfide ores. These results underscore that even a single deposit may record several distinct mineralizing styles, such that the ultimate metal endowment may be cumulative over multiple stages.

Keywords: massive sulfide deposit; Cu–Pb–(±Ag–Au)-bearing quartz–carbonate veins; mineral chemistry; fluid inclusions; ore brines; genetic model

1. Introduction

The Central Jebilet Variscan massif contains several massive sulfide deposits that are interpreted as volcanogenic massive sulfide (VMS)-type deposits and which have been mined for Zn–Pb–Cu commodities, making the province an important base metal source region [1–6]. The Draa Sfar, Kettara and Koudiat Aïcha (Figure 1) deposits are the ones that have been most exploited in recent decades. Mineralization in these deposits consists of pyrrhotite-dominated subvertical lenses enclosed in volcanosedimentary series. Ore lenses experienced variable deformation and metamorphism during the Variscan orogeny.

The genesis of these deposits remains debatable, and hypotheses range from syngenetic to epigenetic genesis (e.g., [4–11]). Remobilization of sulfides is thought to have been the main process that led to ore enrichment during the Variscan metamorphic events in the Central Jebilet massif [10]. Remobilization and upgrading have been emphasized as playing an important role in the Hajjar deposit, Morocco [12], and elsewhere in the world, such as the Iberian Pyrite Belt in Spain [13,14], the Falun pyritic-Zn-Pb-Cu-(Au-Ag) deposit in Sweden [15] and the Kaladawan Zn-Pb-Cu in China [16].

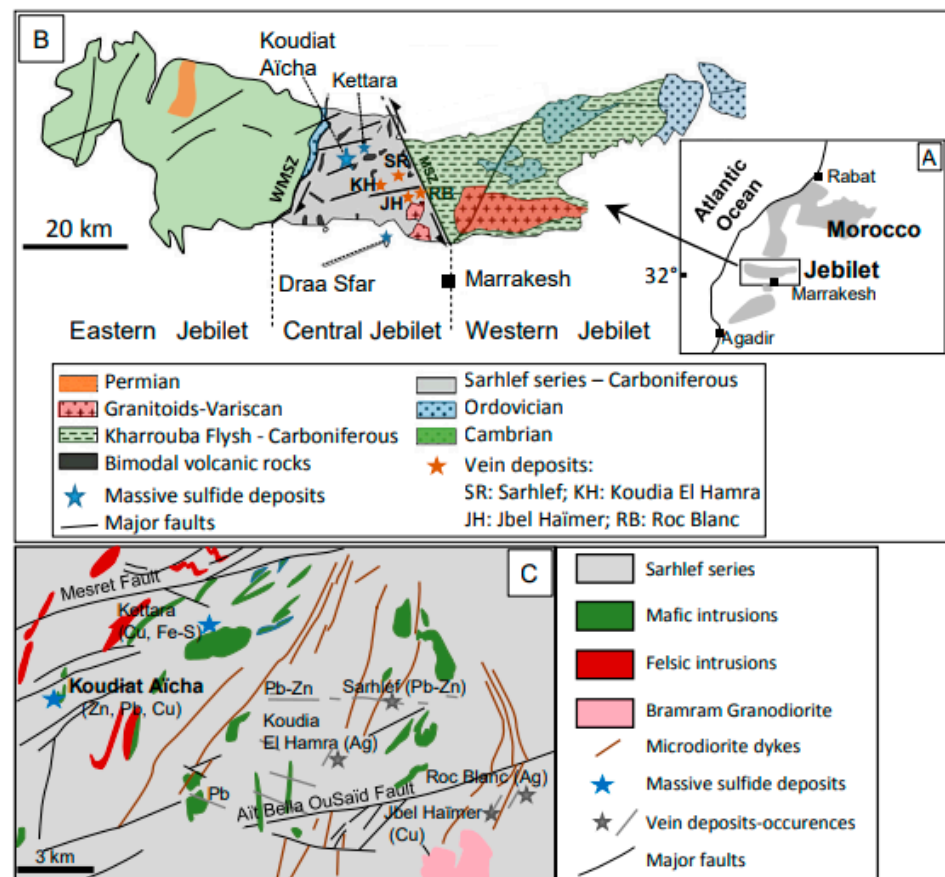


Figure 1. (A) Location of the Variscan massifs in Morocco (in grey: centro-meridional domain). (B) Geology of the Jebilet massif ([1], in [2]) and locations of the main VMS deposits, Koudiat Aïcha, Kettara and Draa Sfar, and the main vein deposits, JH: Jbel Haïmer (Cu), RB: Roc Blanc (Ag), KH: Koudia El Hamra (Ag) and SR: Sarhlef (Pb-Zn), from [1], modified. (MSZ: Marrakesh Shear Zone; WMSZ: West Moroccan Shear Zone; see text for references). (C) Location of Koudiat Aïcha and Kettara massive sulfide deposits and major vein deposits in Central Jebilet (simplified map from [1]).

Lotfi et al. [17] identified a highly deformed vein zone of copper-rich mineralization lateral to the footwall of massive ore lenses in the Koudiat Aïcha deposit. They considered that the Cu-rich ore veins are expressions of a stringer zone proximal to the feeder stockwork, typical of the Besshi-type VMS category. On the other hand, Essaifi et al. [10] reported that such stringer-feeding zones are generally lacking in the Central Jebilet massive sulfide deposits, including Koudiat Aïcha.

Copper-rich quartz vein mineralization (with minor Au and other base metal contents) has been described in the Draa Sfar Zn-Pb-Cu deposit in the Central Jebilet province [11]. These Cu-rich vein ores were suggested to have an epigenetic origin related to syntectonic Cu-Au mineralization systems coeval with the Variscan orogeny and associated metamorphism [11]. In the Iberian pyrite belt, Chauvet et al. [18] suggested that stockwork mineralization in VMS-type deposits may actually result from subsequent deformation and

not necessarily represent a feeder zone. Thus, the nature and origin of stockworks in such massive sulfide environments should be interpreted cautiously [19].

Several studies describe Cu-Zn-Pb ± Ag-Au vein deposits that cut through the Sarhlef volcanosedimentary series in the Central Jebilet (e.g., Pb-Zn- and Cu-bearing vein swarms striking E–W in the Jebilet, [1]; the Roc Blanc and Koudia El Hamra Ag-Cu-Pb-Zn veins, [20,21], respectively; and the Jbel Haïmer Cu-polymetallic occurrences [22,23]). The mineralogical and structural characteristics and the compositions of ore fluids indicate that these base- and precious-metal-bearing veins are post-Variscan. The formation of these deposits has been attributed to the circulation of evaporitic brines during the Triassic extension and the opening of the Central Atlantic Ocean [20].

The genesis of the sulfide vein mineralization at Koudiat Aïcha remains controversial, and questions remain as to whether these veins are related to the massive sulfide mineralization and whether they represent processes of Variscan orogeny or post-Variscan extension. In the present study, we integrate fluid inclusion data with mineralogical and trace-element geochemical data for an updated genetic model of this mineralization. Unravelling the genesis of the Koudiat Aïcha vein ores has implications regarding improving understanding of the metallogeny of the Central Jebilet and may aid new exploration programs.

2. Geological Setting

The Jebilet Variscan massif extends 170 km E–W and 7 to 40 km N–S (Figure 1) and is subdivided into three lithotectonic domains: Western, Central and Eastern Jebilet [1]. Eastern and Central Jebilet are separated by the Marrakesh Shear Zone (MSZ) [24]. The West Moroccan Shear Zone (WMSZ) separates Western from Central Jebilet (e.g., [24,25]) (Figure 1B). The Jebilet series was formed in an intra-continental rift basin [26], where marine sediments deposited in an anoxic environment during the Late Devonian and Early Carboniferous [27,28].

Central Jebilet is dominated by the Carboniferous Sarhlef metasedimentary series (Upper Viséan–Namurian: presence of *Posidonomya becheri* Bronn [29]). This series constitutes a thick succession (≥ 1000 m) of argillites alternating with siltstone, sandstone and locally felsic and mafic tuff, overlain by carbonaceous argillites and limestones [2,4,6,30]. The Sarhlef series is intruded by pre-orogenic bimodal magmatic rocks and calc-alkaline granodioritic plutons [1,2,30,31]. Pre-orogenic mafic–ultramafic rocks are represented by ultramafic cumulates, gabbro and dolerite that did not generate significant contact metamorphism [1]. Cogenetic felsic plutonic rocks (dated at 330.5 ± 0.68 – 0.83 Ma, zircon U–Pb age [32]) are alkaline monzonitic microgranites that induced contact metamorphism reaching the hornblende–hornfels facies [31–33]. Calc-alkaline granodioritic plutons (Figure 1) have been dated at 330.5 ± 0.7 Ma (zircon U–Pb age [32]), 327 ± 4 Ma (Rb–Sr on whole rock [34]). Recent dating of granodiorite gave an age of 358 ± 7 Ma (Tabouchent–Bamega plutons) and 336 ± 4 Ma (Oulad Ouaslam pluton) (U–Pb LA-ICP-MS dating on zircon [35]). The granodiorite intrusions induced contact metamorphism to the pyroxene–hornfels facies [1,36,37]. They are cut by leucogranitic intrusions dated at 297 ± 6 Ma (Bramram pluton [38]) and 295 ± 15 Ma [34] (Rb–Sr method on whole rock), accompanied by contact metamorphism (hornblende–hornfels facies).

From the Late Carboniferous to the Early Permian, the Sarhlef sedimentary series experienced the Variscan orogeny composed of two deformation stages, referred to as D1 and D2 [35]. The D1 compressive event consisted of a likely N–S shortening accompanied by folding and emplacement of allochthonous nappes, coeval with the development of a weak schistosity cleavage, S1, at diagenetic to low-grade metamorphic conditions [35]. The D2 major deformation stage was polyphase and consisted first of a WNW–ESE to NW–SE transpressional crustal shortening that developed NS–N30° E kilometer-size isoclinal folds. High-temperature, low-pressure (HT-LP) metamorphism (M2; greenschist to amphibolite facies [39]) was accompanied by the development of a penetrative cleavage, S2, and was coeval with emplacement of leucogranite intrusions. Then, during the second D2 substage, transpressional shearing induced shear zones at all scales, particularly the multi-kilometer-

sized West Moroccan Shear Zone (WMSZ) and the Marrakesh Shear Zone (MSZ) (Figure 1). The M2 metamorphism, isoclinal folding and shear zones are considered to have occurred within the period of 310–280 Ma [35]. The last substage of D2 led to the development of regional conjugate strike–slip shear zones and brittle reverse faults striking ENE–WSW and NW–SE. The Ait Bella Ousaïd and Mesret faults represent the longest ones (about 15–25 km, respectively; Figure 1C) and strike ENE with a reverse–dextral shearing [35].

Post-orogenic microdiorite dikes and sills striking N–S to N40° E are widespread in the Central Jebilet and may exceed 1 km in length. Microdiorite dykes have an age of 240 ± 10 Ma (as determined by the K–Ar method on kaersutite [40–43]). They are interpreted as having formed during a period of distension (e.g., [2,26,32,42,44]).

Extensional tectonics took place from the Lower Triassic to Post-Kimmeridgian, coeval with the opening of the Central Atlantic Ocean [45–47], and led to the formation of large Tethyan basins (Atlasic basins) in Central Morocco. Thick detrital series with intercalated evaporites and basalt accumulated in Atlasic basins (up to 7–8 km thick [48]). At these times, the Central Jebilet was a relatively shallow area supplied with about 2.4 km of sediments [49]. In the Jebilet massif, the pre-Atlasic extensional period led to the development of E–W fractures and swarms of Cu and/or Pb–Zn–(Cu) quartz–carbonate veins [1]. During the Atlasic orogeny (Eocene), pre-existing structures were reactivated while new E–W-striking faults developed in the Jebilet [50].

3. The Koudiat Aïcha Deposit

Koudiat Aïcha is a pyrrhotite-rich Zn–Pb–Cu deposit located about 36 km northwest of Marrakesh, Morocco (Figure 1). It was discovered in 1963 through a combination of geophysical studies (an airborne electromagnetic anomaly) and drilling, and production began in 2016. Ore reserves range from 3 to 5 Mt grading, 3 wt.% Zn, 1 wt.% Pb and 0.6 wt.% Cu, and significant Au and Ag grades of up to 1.8 ppm for Au and 114 ppm for Ag are found locally in drilling samples [17].

The Koudiat Aïcha ore bodies consist presently of three subvertical parallel-to-subparallel lenses with a general N–S orientation, and the deposit is still expanding. The lateral N–S extent of the lenses ranges from 100 to 500 m, with a vertical extent ranging from 300 to at least 600 m and a thickness ranging from a few meters to ~20 m (Figure 2). Ore lenses are hosted in metasedimentary rocks comprising metamorphosed grey-to-black carbonaceous argillites with rhythmic intercalations of sandy argillite in sandstone layers (0.5–1 m thick) from the Sarhlef series (Figure 2), considered as the footwall to the west [17]. Sandy argillite and sandstone layers form several N–S trending crests that crop out in the Koudiat Aïcha area. Black argillites with locally fossiliferous limestone at the top form the hanging wall to the east (Figure 2, [17]). Magmatic rocks are predominantly gabbro, which forms several paraconcordant N–S sills a few meters in thickness, together with a larger gabbro body of several tens of meters (Figure 2) and local tuffs, rhyodacite and minor microgabbros, diorite and dolerite that intrude into the argillites [51]. Argillite layers (referred to as schist hereafter) together with gabbro dikes and sills experienced Variscan deformation and dip steeply to the east, constituting the eastern flank of an anticline, and both show an N–S to NNE schistosity cleavage [17,51], attesting to their pre-orogenic deposition. Ore lenses are generally parallel and paraconcordant with the schist and sandstone layers, but locally show deformed contacts characterized by faults and sheared or even mylonitized zones that separate ore lenses from host schist. The contact zones experienced hydrothermal alteration that consisted mainly of chloritization, sericitization and silicification. Ore bodies are exposed to the surface by several N–S multi-meter sized discontinuous lineaments of strongly oxidized gossan (Figure 2), which mainly coincide with the sandy schist layers and sandstone crests. Hematite, goethite and malachite are the major minerals of the gossan, with lesser amounts of azurite and chrysocolla.

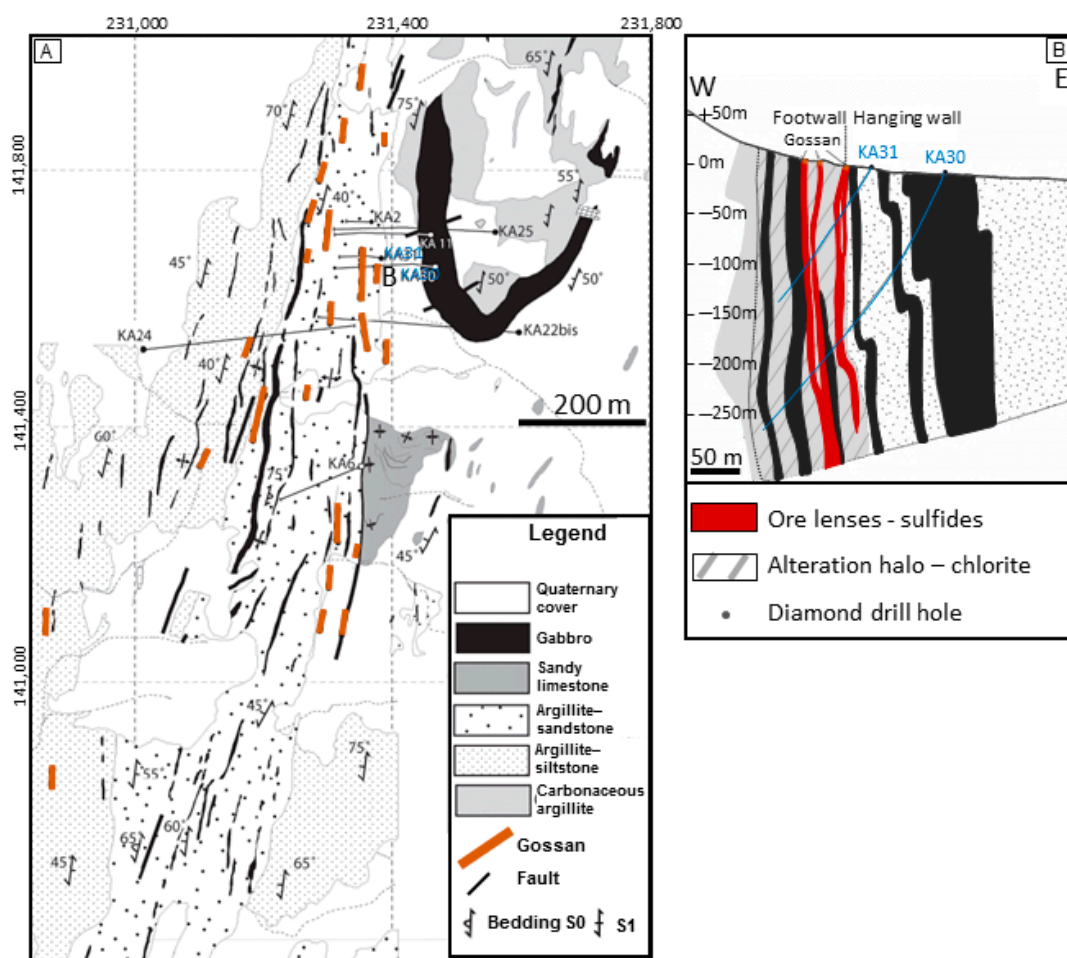


Figure 2. (A) Geological map of the Koudiat Aïcha area [17] (modified). (B) Cross section along two drillings, KA31 and KA32, cutting across the ore lenses [17] (modified); see (A) for drilling locations.

4. Methods

Sampling was conducted underground at the main level of -250 m and in adits that intersect orebody lenses. Thirty thin and thick sections were prepared for petrographic and scanning electron microscopy (SEM) analysis at Cadi Ayyad University, Marrakesh, Morocco.

The chemical compositions of the different sulfide minerals were determined using an electron probe microanalyzer (EPMA; JEOL JXA-8200 super probe) and a laser ablation inductively coupled plasma mass spectrometer (ICP-MS) system (Geo Las Pro-AttoM, Nu-Instruments) at the GEOMAR-Helmholtz Center for Ocean Research in Kiel, Germany. The analytical conditions for the quantitative analyses of sulfides by EPMA were: 15 kV accelerating voltage, 30 nA probe current, beam diameter of ~ 1 μm and counting times of 20–40 s and 10–20 s for peak and background, respectively. The standard materials used included natural chalcopyrite (for S, Cu, Fe), sphalerite (Zn), galena (Pb), cassiterite (Sn), Bi_2Se_3 (Bi, Se), AgTe (Ag, Te), GaAs (As), CdS (Cd), InSb (Sb) and NiO (Ni) with known compositions.

For spot analyses of different sulfide phases, we used a 193 nm Excimer laser ablation system (Coherent, GeoLasPro) coupled to a double-focusing, high-resolution magnetic sector mass spectrometer (Nu Instruments, AttoM) under hot plasma conditions ($\text{NAI} = 29.7\text{--}30.6$, $\text{ThO}/\text{Th} = 0.018\text{--}0.038\%$; details in [52]). Spot analyses were performed using 30 s of ablation under helium carrier gas at a laser repetition rate of 5 Hz, using spot diameters between 32 and 44 μm . The energy density was 2 J cm^{-2} for ablating sulfides and 5 J cm^{-2} for ablating silicates. The USGS glass standard BHVO-2G [53], the USGS sulfide standard MASS-1 [54] and the synthetic sulfide standard PGE-Ni7b [55] were used

as reference materials. NISTSRM610 [56] was used for mass calibration, but due to the absence of suitable reference values for S, Ru, Os, Ir and Hg MASS-1 was used additionally to calibrate S, Ir and Hg, and PGE_Ni7b was used to calibrate Ru and Os. There were 50–80 s of gas background data collected prior to each ablation. Data were corrected for the following interferences: $^{65}\text{CuH}^+$ on $^{66}\text{Zn}^+$, $^{63}\text{Cu}^{40}\text{Ar}^+$ on $^{103}\text{Rh}^+$, $^{65}\text{Cu}^{40}\text{Ar}^+$ on $^{105}\text{Pd}^+$ and $^{115}\text{Sn}^+$ on $^{115}\text{In}^+$. The exact argide and hydride formation rates were determined by ablating elemental Cu (linescan, 60–120 s, 32 μm , 5 J cm^{-2}). Data evaluation was performed by applying the linear regression slope method, as detailed in [57].

Twenty doubly polished wafers were prepared for fluid inclusion studies. Fluid inclusion petrography and classification were based on contents of aqueous (w) and carbonic (c) fluids and on modes of total homogenization (L: liquid, V: vapor). Thus, fluid inclusions rich in molecular gases are referred to as Lc and Vc to indicate homogenization to the carbonic liquid phase versus the vapor phase, respectively; aqueous carbonic fluid inclusions that homogenize to the liquid phase are noted as Lwc; and aqueous fluid inclusions that homogenize to the liquid phase are referred to as Lw [58]. Halite-bearing aqueous inclusions are referred to as Lwh (w: water, h: halite).

Microthermometric measurements were performed using a Linkam THSMG600 freezing–heating stage [59]. Abbreviations for microthermometric data presentation follow the conventions set forth in [60] (Table 1).

Table 1. Abbreviations for microthermometric data [60].

Symbol	Definition
$T_{m\text{CO}_2}$	Melting temperature of dry ice (solid CO_2) in inclusions rich in molecular gases
$T_{h\text{CO}_2}$	Homogenization temperature of the carbonic phase in inclusions rich in molecular gases
T_e	Temperature at which the first liquid appears in inclusion during low-temperature measurements
$T_{m\text{hh}}$	Hydrohalite melting temperature
$T_{m\text{ice}}$	Ice melting temperature
$T_{m\text{cl}}$	Clathrate melting temperature
$T_{h(L\rightarrow V)}$	Total homogenization temperature (L meaning homogenization to the liquid phase, V meaning homogenization to the vapor phase)
$T_{m\text{h}}$	Halite (NaCl) melting temperature, $T_m\text{NaCl}$ for Roedder [60]

The precision of the phase transition at low temperatures was from +0.2 °C (below 0 °C) to +0.4 (for very low temperatures below −100 °C). Precision was ~1 to 2 °C for the liquid–vapour homogenization and melting temperature of halite. Salinity calculations for the aqueous fluid inclusions (H_2O –NaCl system) were made using equations from [61] based on $T_{m\text{ice}}$ or on $T_{m\text{h}}$, and for the H_2O –NaCl– CaCl_2 system using data from [62] by combining $T_{m\text{ice}}$ and $T_{m\text{h}}$ data.

5. Mineralogy, Paragenesis and Trace Elements

Ore textures and microanalytical analyses of the main sulfide minerals (SEM, EPMA, LA-ICP-MS) suggest overprinting distinct phases of mineralization. The main sulfide phases include, in order of abundance: pyrrhotite, pyrite, sphalerite, chalcopyrite and galena. Orebodies are massive, semi-massive, banded, breccia and vein infillings. The petrographic studies revealed a general three-stage paragenetic sequence for the Kouadiat Aïcha deposit (Table 2).

Table 2. Paragenetic sequence for the Koudiat Aïcha deposit.

Stages	Sedimentary?	Ore Stage I	Vein-Banded-Breccia-Shear Zone - Ore Stage II			Cu-Polymetallic Vein Ore Stage III	Supergene
		Fe-Zn	Barren	Fe-As	Fe-Zn	Cu-Pb-(Sb-Sn-Ag-Au, Fe, Bi, Te, Se)	
Minerals		Fe-Zn	Barren	Fe-As	Fe-Zn	Cu-Pb-(Sb-Sn-Ag-Au, Fe, Bi, Te, Se)	Cu - Fe
Pyrite 1	—						
Pyrrhotite 1		—					
Chlorite 1		— ?					
Sphalerite 1		—					
Quartz 1 (veins)			—				
Biotite (chloritized)			—				
Ti-oxides			---				
Pyrite 2				—			
Arsenopyrite				—			
Chalcopyrite						
Pyrrhotite 2					—		
Muscovite					—		
Chlorite 2					—		
Sphalerite 2					—		
Mg-Siderite (veinlets)						—	
Ferroan Dolomite - Calcite (veins)						—	
Chalcopyrite						—	
Stannite						—	
Galena						—	
Ag-Tetrahedrite-Freibergite						—	
Boulangerite						—	
Sulfosalts (Pb-Sb±Fe±Cu)						—	
Natives : Ag-Au alloy						---	
Argentite						---	
Ferroan dolomite (veinlets)						—	
Chlorite 3						—	
Malachite							—
Chrysocolla							---
Fe-Oxides/hydroxides							—

5.1. Ore Stage I

The first ore stage represents the stratabound massive sulfide-type mineralization and generally lacks transparent gangue minerals that could be used for fluid inclusion analysis, as described below. This massive sulfide-type ore consists primarily of iron sulfides (pyrite and pyrrhotite) as well as subordinate sphalerite. Pyrite 1 is sporadically present as corroded anhedral grains that form microlayers conformable to banding of the host argillites.

Pyrrhotite 1, antiferromagnetic, is the major mineral in the early massive ore (Figure 3A–C), commonly overgrows anhedral pyrite 1 microdomains and microlayers and is highly deformed (Figure 3B). Pyrrhotite 1 is associated with dark-red Fe-rich sphalerite 1 (Figure 3C,F,L), and both form an early paraconcordant folded and locally brecciated ore (Figure 3C). Pyrite 1 and pyrrhotite 1 contain traces of Co and Ni (<1 wt.%).

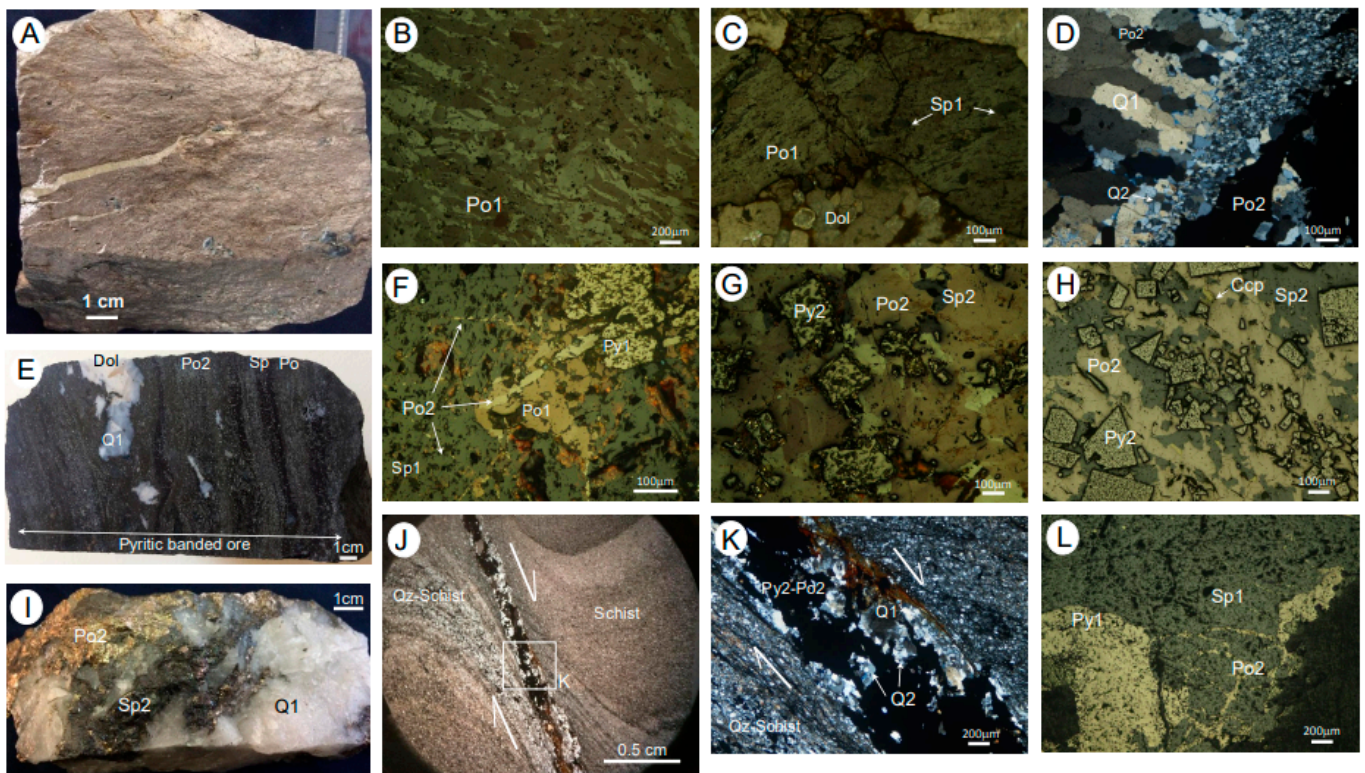


Figure 3. Mineralogy of Koudiat Aïcha: early stages. (A) Hand specimen showing the pyrrhotite-dominated massive ore. Optical microscope observation: (B) Deformed pyrrhotite 1 from massive ore. (C) Brecciated massive early ore with pyrrhotite 1 and sphalerite 1 empacked in dolomite matrix. (D) Quartz 1 vein crosscutting sandy schist and quartz 2, pyrrhotite 2 filling quartz 1 veins and sandy schist. (E) Hand specimen showing banded “pyritic ore” enveloping quartz 1 fragments overgrown by dolomite. (F) Pyrrhotite 1, pyrite 1 and sphalerite 1 crosscut by pyrrhotite 2. (G,H) Pyrite 2 overgrown by pyrrhotite 2 and sphalerite 2. (I) Hand specimen showing ore breccia of quartz 1 fragments enveloped by pyrrhotite 2 and sphalerite 2. (J) Microshear zone crosscutting schist and sandy microlayers and infilled with quartz 1–sulfide–chlorite–mica. (K) Detail of picture (J) Microshear zone infilled with quartz 1 and quartz 2, pyrite 2, pyrrhotite 2 and crosscutting sandy schist microlayers. (L) Pyrrhotite 2 enveloping and crosscutting sphalerite 1 and pyrite 1 in ore breccia. Po: pyrrhotite, Sp: sphalerite, Py: pyrite, Ccp: chalcopyrite, Q1: quartz, Dol: dolomite, Qz-schist: sandy schist.

5.2. Ore Stage II

Quartz 1–biotite veins (several centimeters in thickness at most and in general <1 m in extent) crosscut schist and magmatic rocks (Figure 3D,J,K). Quartz 1 is intensively sheared and brecciated (Figure 3D,E,I), while biotite is consistently chloritized. Quartz 1–biotite veins are initially barren and generally show reworking and reopening, then infilling with later minerals (Figure 3D,J,K). Pyrite 2, present as euhedral crystals, is the main mineral of a massive to submassive and banded ore named “pyritic ore” (Figure 3E), where it is overgrown by later minerals (Figure 3G,H). Pyrite 2 locally envelops brecciated Q1 fragments (Figure 3E) and fills the cores of early quartz 1 veins. Pyrite 2 contains several trace elements in high concentrations (As and Co average values: 2250 ppm and 320 ppm, respectively). Lead, Ni and Sb occur with relatively high contents (up to 243 ppm for Pb, 71 ppm for Ni and 122 ppm for Sb; Table 3). Arsenic is correlated with Ni and Co (Figure 4A,B), Sb with Bi. Molybdenum and Mn are consistently present in relatively low concentrations (average Mo: 7 ppm, Mn: 6 ppm). Several other trace elements were occasionally detected, mainly Se and Ag, reaching 74 ppm and 23 ppm, respectively, while

Bi reached 18 ppm. Copper, Zn, Cd, In, Sn, Te, Ge, Ga, Tl and Au were sporadically detected in low amounts (mostly <10 ppm; Table 3).

Table 3. LA-ICP-MS (in bold font) and EPMA (in italic font) data for the major sulfides at Koudiat Aïcha (stage II and stage III). Averages in brackets, < LOD: below detection limit, traces: close to the LOD. EPMA data in wt.%; LA-ICP-MS data in ppm.

	Stage II			Stage III	
	Pyrite 2	Pyrrhotite 2	Sphalerite 2	Chalcopyrite	Galena
S	52.07–54.84 (53.29)	38.03–42.5 (39.64)	30.80–32.88 (31.76)	30.29–35.9 (33.39)	12.17–14.93 (13.90)
Fe	45.71–46.6 (46.34)	57.04–62.29 (59.95)	2.36–3.65 (3.04)	28.24–33.56 (30.91)	<LOD – 2.89
Zn	<LOD – 13	<LOD – 23	62.26–64.49 (63.29)	266–632 (419)	<LOD – 19
Cu	<LOD – 2	0–3	32–207 (79)	33.34–37.63 (35.16)	<LOD – 17
As	836–8490 (2550)	<LOD – 82	1–4 (2)	2–30 (12)	<LOD – 9
Pb	15–243 (141)	5–132 (109)	2–452 (51)	40–596 (235)	84.09–85.34 (84.5)
Mn	2–33 (6)	1–31 (12)	1.44–1.69 (1.57)	2–139 (29)	<LOD – 2.3
Co	6–572 (320)	<LOD – 1	<LOD – 2 (1)	<LOD – 16 (6)	traces
Ni	8–71 (27)	11–34 (22)	<LOD–17 (10)	4–198 (83)	2–22 (9)
Ga	<LOD – 2	<LOD	17–26 (21)	3–21 (8)	<LOD – 9
Ge	<LOD	<LOD	<LOD – 5	9–83 (37)	<LOD – 10
Se	<LOD – 74	<LOD – 30	<LOD – 18 (11)	<LOD – 163	94–176 (123)
Mo	3–13 (7)	10	<LOD – 5 (3)	10–54 (32)	6
Ag	<LOD – 23 (9)	1–9 (4)	6–24 (12)	158–291 (212)	705–1136 (963)
Cd	<LOD – 4 (3)	<LOD – 4	1825–2197 (1943)	<LOD – 6	<LOD – 3
In	traces	traces	55–71 (60)	8–16 (12)	<LOD – 1
Sn	1	<LOD – 1	1–5 (3)	240–473 (353)	76–133 (103)
Sb	<LOD – 122 (24)	<LOD – 19 (5)	<LOD – 21 (8)	31–77 (56)	130–210 (177)
Te	<LOD – 6	<LOD – 4	<LOD – 2 (1)	3–15 (11)	8–9 (9)
Au	<LOD – 2	<LOD	<LOD – 1	<LOD – 2	<LOD – 4 (1)
Hg	traces	<LOD	1–4 (3)	<LOD – 2	<LOD – 1
Tl	<LOD – 3	<LOD – 2 (1)	traces	1–6 (3)	57–78 (70)
Bi	<LOD – 18 (6)	<LOD – 9 (2)	<LOD – 1	3–9 (4)	1903–2554 (236)

Anhedral arsenopyrite, present as scarce corroded crystals and microdomains of several tens of micrometers, is consistently associated and likely synchronous with pyrite 2. Euhedral arsenopyrite (a few micrometers in size) forms locally polycrystalline microdomains (Figure 5B,D) that seem to result from the recrystallization of corroded arsenopyrite. Euhedral arsenopyrite microcrystals contain trace elements, mainly Cu, Zn, Co and Sb (0.1–0.2 wt.%). Nickel and Bi are below the detection limit (LOD).

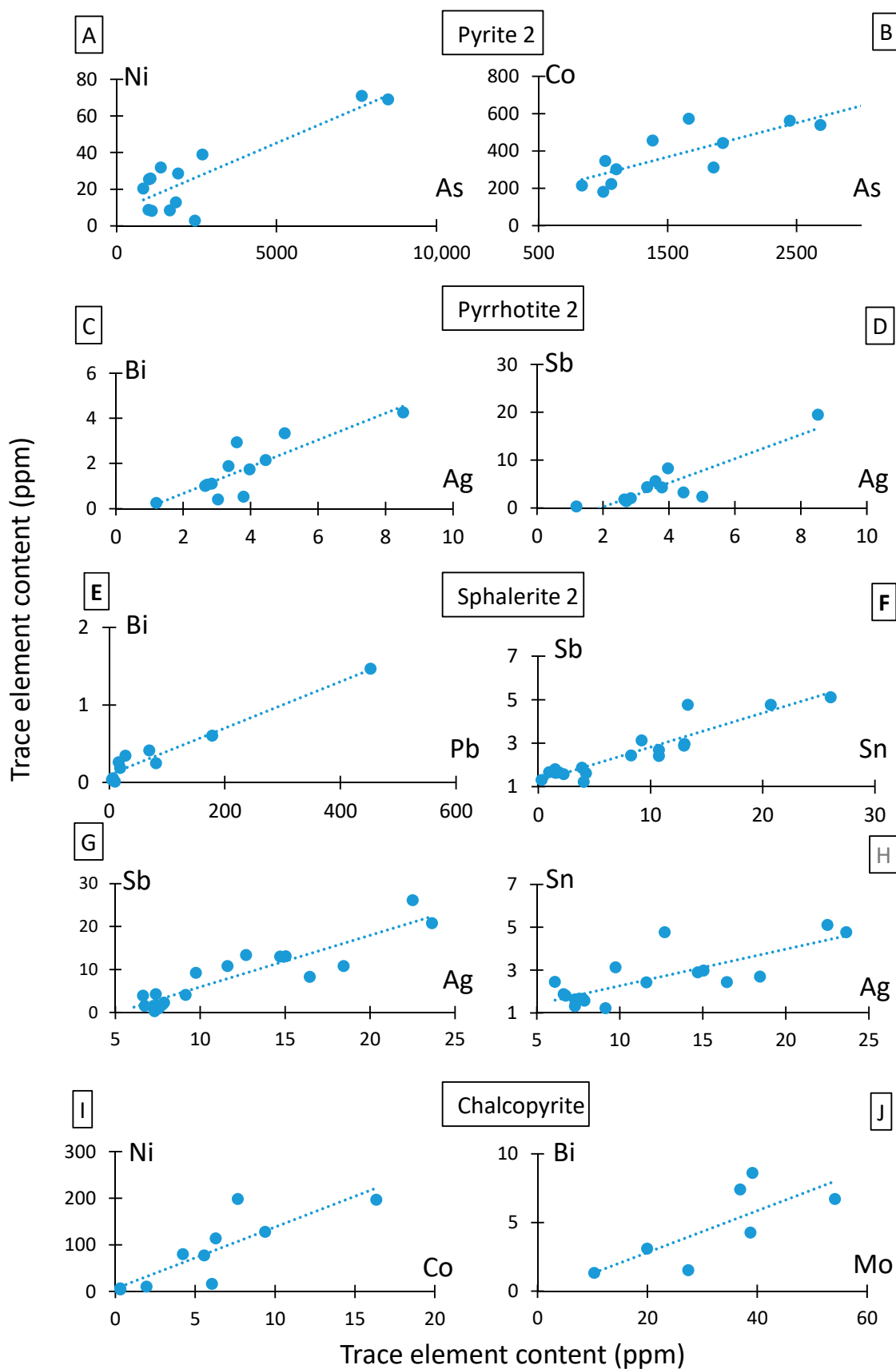


Figure 4. Correlation of trace elements detected using LA-ICP-MS analysis in major minerals from Koudiat Aïcha (from stage II: pyrite 2, pyrrhotite 2 and sphalerite 2; from stage III: chalcopyrite). Data are in ppm. Stage II. (A,B) Pyrite 2, (C,D) Pyrrhotite 2, (E–H) Sphalerite 2; Stage III: (I,J) Chalcopyrite.

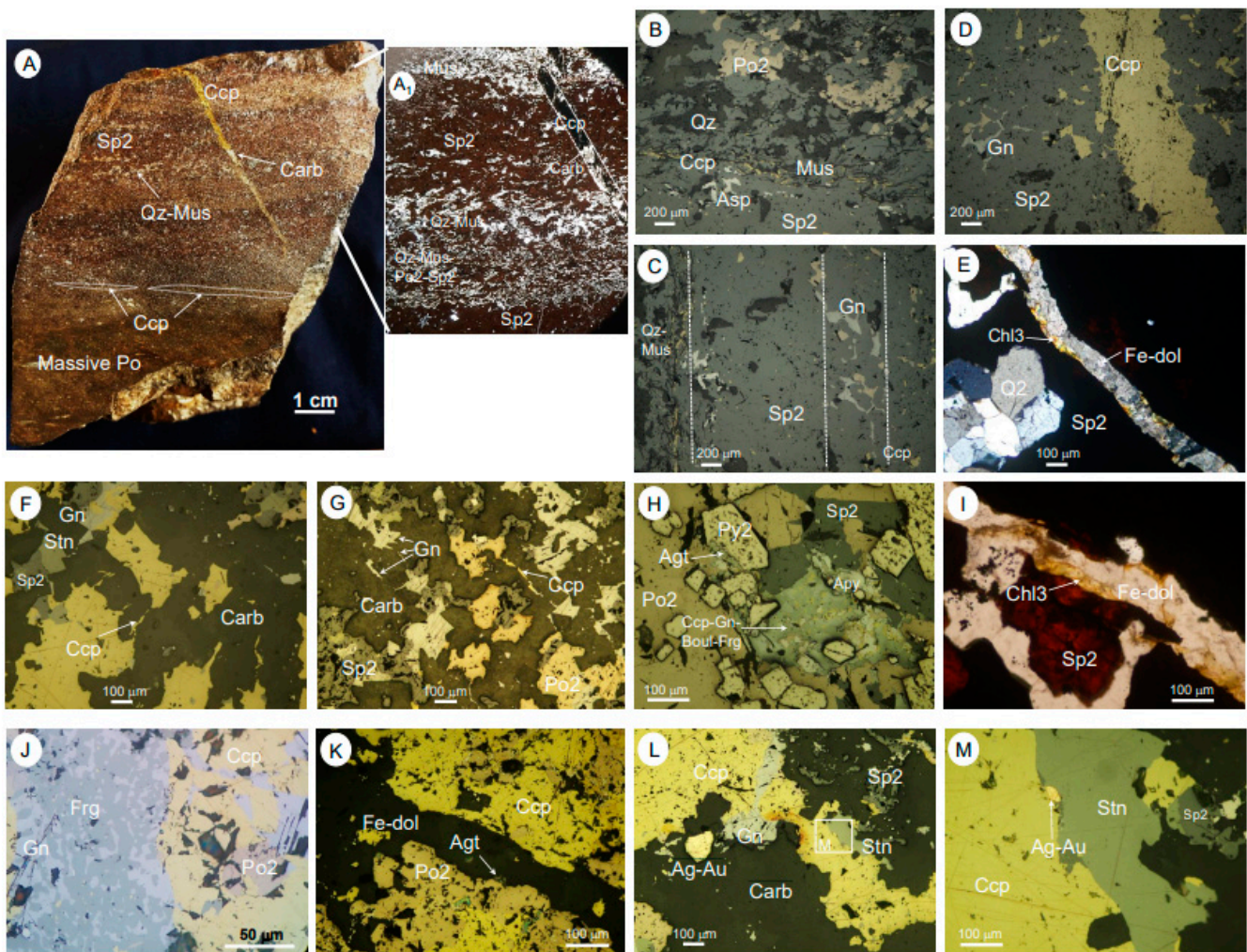


Figure 5. (A) Hand specimen showing banded sphalerite-rich ore with alternations of layers of pyrrhotite, quartz–muscovite, and thinner layers of late chalcopyrite and galena, with a crosscutting carbonate–chalcopyrite veinlet. (A₁) Detail of (A) observed with binocular viewing. Optical microscope observations: (B–D) Details of (A). (E) Quartz 2 associated with sphalerite 2 crosscut by late minerals. (F,G) Chalcopyrite, stannite and galena crosscutting carbonates (calcite + dolomite) and packing pyrrhotite 2 and sphalerite 2 fragments/crystals. (H) Pyrite 2, euhedral arsenopyrite and pyrrhotite 2 enveloped in sphalerite 2—all overgrown by a late sulfide assemblage (chalcopyrite, boulangerite–galena–Ag-tetrahedrite/freibergite and argentite). (I) Sphalerite 2 crosscut by a veinlet infilled with chlorite 3 and late ferroan dolomite. (J) Myrmekitic texture of galena and synchronous Ag-tetrahedrite–freibergite overgrowing pyrrhotite 2 and chalcopyrite. (K) Late Fe-dolomite veinlet with argentite crosscutting a pyrrhotite 2 layer and chalcopyrite. (L,M) Late assemblage (stage III): chalcopyrite overgrown by stannite and galena and a microcrystal of Ag–Au alloy in (M) Ag–Au alloy in fissure between chalcopyrite and stannite. Po: pyrrhotite, Sp: sphalerite, Py: pyrite, Asp: arsenopyrite, Ccp: chalcopyrite, Stn: stannite, Gn: galena, Boul: boulangerite, Frg: Ag-tetrahedrite/freibergite, Agt: argentite, Fe-dol: later ferroan dolomite, Chl: chlorite.

Pyrrhotite 2 is the most abundant sulfide at Koudiat Aicha, identified by a quasi-consistent ferromagnetism (monoclinic pyrrhotite [63]) and low degree of deformation (Figure 3G) compared to pyrrhotite 1. Pyrrhotite 2 forms interbedded layers with pyrite 2 and sphalerite 2 in banded ores, occurs as anhedral microdomains in semi-massive ore and forms a matrix in which euhedral pyrite 2 is coated in “pyritic ore” (Figures 3E,G,H and 5A,B). In addition, pyrrhotite 2 fills the core of quartz 1 veins (Figure 3D) and centimeter-sized fractures and shear zones (Figure 3J,K). In veins and shear zones, pyrrhotite 2 is accom-

panied by sheared quartz 1, clear polygonal quartz 2 (Figure 3D,J,K) (likely resulting from deformation/recrystallization of quartz 1), chloritized biotite, brecciated pyrite 2, fragmented rutile and sporadic elongated crystals of Ti-Si-(Ca) oxide (probably titanite). Euhedral chlorite 2 and muscovite commonly envelop and crosscut pyrrhotite 2 in fractures and shear zones. Finally, in a common ore breccia type, pyrrhotite 2 envelops quartz 1 fragments (Figure 3I), pyrite 2, anhedral and euhedral arsenopyrite crystals, and commonly overgrows or crosscuts pyrrhotite 1 and sphalerite 1 (Figure 3F,L). Disseminations of pyrrhotite 2–chlorite 2–muscovite preferably fill the schistosity planes in sandy layers of the host schist, particularly in common quartz-rich microdomains. Pyrrhotite 2 contains several trace elements in significant amounts. Lead, Ni, Mn and Sb are consistently present and reach levels of 131 ppm, 34 ppm, 31 ppm and 19 ppm, respectively; Ag and Bi maximum contents are 9 ppm (Table 3). Several trace elements are occasionally detected (generally less than a few tens of ppm for As, Se and Zn and close to the LOD for Cu, Te, Co, Tl and Sn; Table 3). Silver is correlated with Bi and Sb (Figure 4C,D).

Sphalerite 2 is the third most-abundant sulfide (after pyrrhotite and pyrite) and forms the main Zn mineralization, mostly present as banded ore (Figure 5A). The latter consists of relatively thick sphalerite layers (several centimeters) alternating with thinner layers of pyrrhotite 2 plus silicates (quartz–muscovite–chlorite; Figure 5A–C). Sphalerite 2 envelops all the minerals described above and infiltrates early banded, semi-massive, breccia and vein/shear zone ores (Figure 3H,I). It most commonly postdates deposition of chlorite 2 and muscovite and was probably deposited synchronously with quartz 2 (Figure 5E). Sphalerite 2 contains Fe (2.36–3.65 wt.%), and the deep-brown color of sphalerite 2 may suggest the partial substitution of Zn by Fe and/or Mn [64,65], but no anti-correlation is present between Fe and Zn contents. Sphalerite 2 is also Mn- and Cd-rich (Mn average: 1.57 wt.%, Cd average: 1943 ppm). Cadmium concentrations in sphalerite 2 may reflect $\text{Cd}^{2+} \leftrightarrow \text{Zn}^{2+}$ substitution [64,66], although no evident anti-correlation was observed between chemical contents of Zn and Cd. Sphalerite 2 contains significant concentrations of Pb, Cu, In, Ga, Ag, Sb, Se and Ni (up to 452 ppm, 207 ppm, 71 ppm, 26 ppm, 24 ppm, 21 ppm, 18 ppm and 17 ppm, respectively; Table 3). Germanium content is low (<LOD to 5 ppm). Cobalt (<2 ppm) is correlated with Ni. Lead is strongly correlated with Bi (Figure 4E), which is in turn slightly less correlated with Mo. Ag is strongly correlated with Sb, which is correlated with Sn (Figure 4F,G). Indium does not correlate with Cu, ruling out the coupled ($\text{Cu}^+ \text{In}^{3+} \leftrightarrow 2\text{Zn}^{2+}$ substitution [67]); therefore, the Cu concentration may reflect the presence of chalcopyrite and/or stannite minute inclusions from a later stage in sphalerite 2. Even though Sn content is low (≤ 5 ppm), it is strongly correlated with Sb and slightly less so with Ag (Figure 4H). Tin correlation with Ag may suggest a ($2\text{Ag}^+ \text{Sn}^{4+} \leftrightarrow 3\text{Zn}^{2+}$ coupled substitution [64]. Ag does not correlate with Hg, which is consistently present at relatively low concentrations (up to 3 ppm), nor with Au, which presents low concentrations close to the LOD.

5.3. Ore Stage III (Cu-Polymetallic Ore Veins)

Mg-siderite was the first mineral to form in the late fissural stage, followed by calcite and ferroan dolomite veins and veinlets. Carbonates crosscut, envelop and infiltrate massive, early ore breccia and banded sulfide ores, including pyrrhotite, pyrite, arsenopyrite, sphalerite, quartz, chlorite and muscovite (Figure 3C,E and Figure 4A,F,G), and locally terminate in geodes. Furthermore, carbonate minerals fill interstitial spaces in sandy argillites and sandstone layers and overgrow sulfide disseminations.

Late sulfides grow on calcite and ferroan dolomite and fill microfractures (Figures 4 and 6). Chalcopyrite overgrows and locally replaces calcite–dolomite and early sulfides in massive, semi-massive, breccia and banded ores and early fracture–shear zones (Figure 5F,G,K) and fills microfractures crosscutting them (Figure 5A,D). Stannite, followed by relatively abundant galena, rim and crosscut chalcopyrite (Figure 5F,L), pyrrhotite 2 and sphalerite 2 crystals filling early fractures and shear zones and occurring as fragments in carbonate microdomains (Figure 5C,D,F,G,L). In the current state of knowledge of Kouadiat Aïcha miner-

alogy, it is not ruled out that a small amount of sphalerite may be related to stage III. Galena is synchronous with boulangerite and a Ag-Cu-Sb-Fe sulfosalt (Ag-tetrahedrite–freibergite; Figure 6A–E,G) with which it commonly displays a myrmekitic texture (Figure 5J).

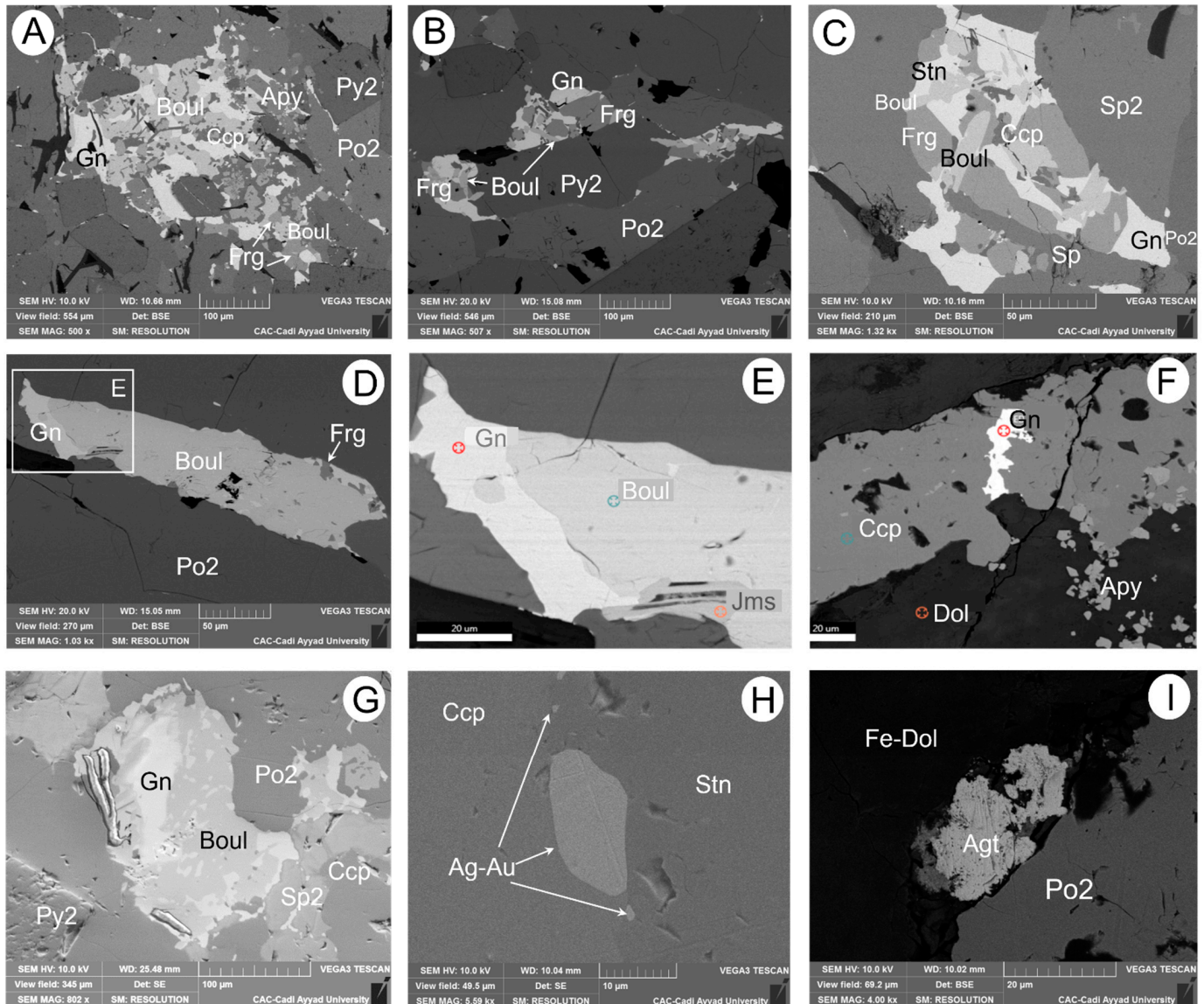


Figure 6. Ore minerals from Koudiat Aïcha observed by scanning electron microscopy. (A,B,C) Sulfides from ore stage II (pyrite 2, pyrrothite 2, arsenopyrite 2) overgrown by sulfides from stage III (chalcopyrite, galena, boulangerite, Ag-tetrahedrite-freibergite). (D,E) Late assemblage (galena, boulangerite, Ag-tetrahedrite-freibergite, jamesonite) overgrowing pyrrothite 2. (E) Detail of (D,F) Dolomite crosscut by veinlet of chalcopyrite itself crosscut by galena. (G) Myrmekitic texture of galena-boulangerite. (H,I) Ag minerals: Ag-Au alloy in a fissure bordering chalcopyrite and stannite (H) and argente in late Fe-dolomite vein crosscutting pyrrothite 2. Po: pyrrothite, Sp: sphalerite, Py: pyrite, Asp: arsenopyrite, Ccp: chalcopyrite, Stn: stannite, Gn: galena, Boul: boulangerite, Frg: Ag-tetrahedrite/freibergite, Jms: Jamesonite, Ag-Au: Ag-Au alloy, Agt: argente, Fe-dol: later ferroan dolomite.

Several minor sulfosalts form at this later stage and comprise Pb-Sb-Fe-sulfide (presenting jamesonite microscope characteristics; Figure 6E), sporadic Pb-Cu-Sb sulfide (bournonite or cuprian boulangerite) and Fe-Sb-sulfide (probably gudmundite). Locally, Ag-Au alloys (~46 to 69 wt.% Ag, ~31 to 54 wt.% Au) crystallize together with galena in microfractures crosscutting chalcopyrite and stannite (Figure 5L,M,H). Late ferroan dolomite veinlets crosscut early Mg-siderite and calcite-Fe-dolomite assemblages as well as sphalerite 2-quartz 2 and chalcopyrite (Figure 5E,I,K). Late Fe-dolomite veinlets are lined with undeformed chlorite 3 (Figure 5E,I) and contain argentite (Figures 4K and 6I), constituting, together with Ag-tetrahedrite-freibergite and Ag-Au alloys, the main Ag minerals.

Microanalyses of chalcopyrite revealed an abundance of several trace elements consistently present (average contents: 419 ppm Zn, 353 ppm Sn, 235 ppm Pb, 212 ppm Ag, 83 ppm Ni, 56 ppm Sb, 29 ppm Mn, 12 ppm In, 6 ppm Co; Table 3). Several other elements were commonly detected (up to 83 ppm of Ge, 22 ppm of Ga, 30 ppm of As, 54 ppm of Mo and 18 of ppm Te; Table 3). Selenium (up to 163 ppm), Cd, Au and Hg (<10 ppm) were occasionally detected. Cobalt is correlated with Ni (Figure 4I), while Mo is slightly correlated with Bi (Figure 4J) and Zn with Cu.

Stannite contains detectable concentrations of Te and Se, and boulangerite presents traces of Cu, Te and Se.

Galena is rich in Bi and Ag (up to 2554 ppm and 1136 ppm, respectively) and contains relatively high concentrations of Sb, Se, Sn and Tl (up to 210 ppm, 176 ppm, 133 ppm and 78 ppm, respectively; Table 3). Lower concentrations of Ni, Cu, Te, Mn, Mn, Co, Zn, Mo, Ga, Ge, Cd, In and Hg were detected in galena (<LOD to 20 ppm; Table 3). Bismuth is strongly correlated with Ag, Tl and Te, Sb with Te, Ag with Tl, and, finally, Ag with Tl and Te. Indium is anti-correlated with Sn.

5.4. Trace Element Distribution

LA-ICP-MS analyses of the mineralized quartz and carbonate vein samples (Table 3) revealed pyrite 2 as the preferred host mineral for As and Co as trace elements; sphalerite 2 for Mn, Cd, Cu, In, Ga and Hg; chalcopyrite for Zn, Ge, Mo, Sn and Te; and galena for Bi, Ag, Sb and Tl. Thus, As, Co, Cd and In are trace elements characterizing vein stage 1 (pyrite 2-pyrrhotite 2 and sphalerite 2), while Bi, Sn, Sb, Se (Figure 7), Ge, Te and Tl are almost exclusively contained as trace elements in minerals from vein stage 2 (i.e., chalcopyrite, galena, stannite and boulangerite assemblages). Silver is a major trace element characterizing vein stage 2 (in chalcopyrite and mainly enriched in galena; Figure 7), while Au occurs in amounts that are lower to slightly close to the LOD in all vein stages (<5 ppm). Lead and Ni (Figure 7) are present as significant trace elements in minerals from vein stages 1 and 2.

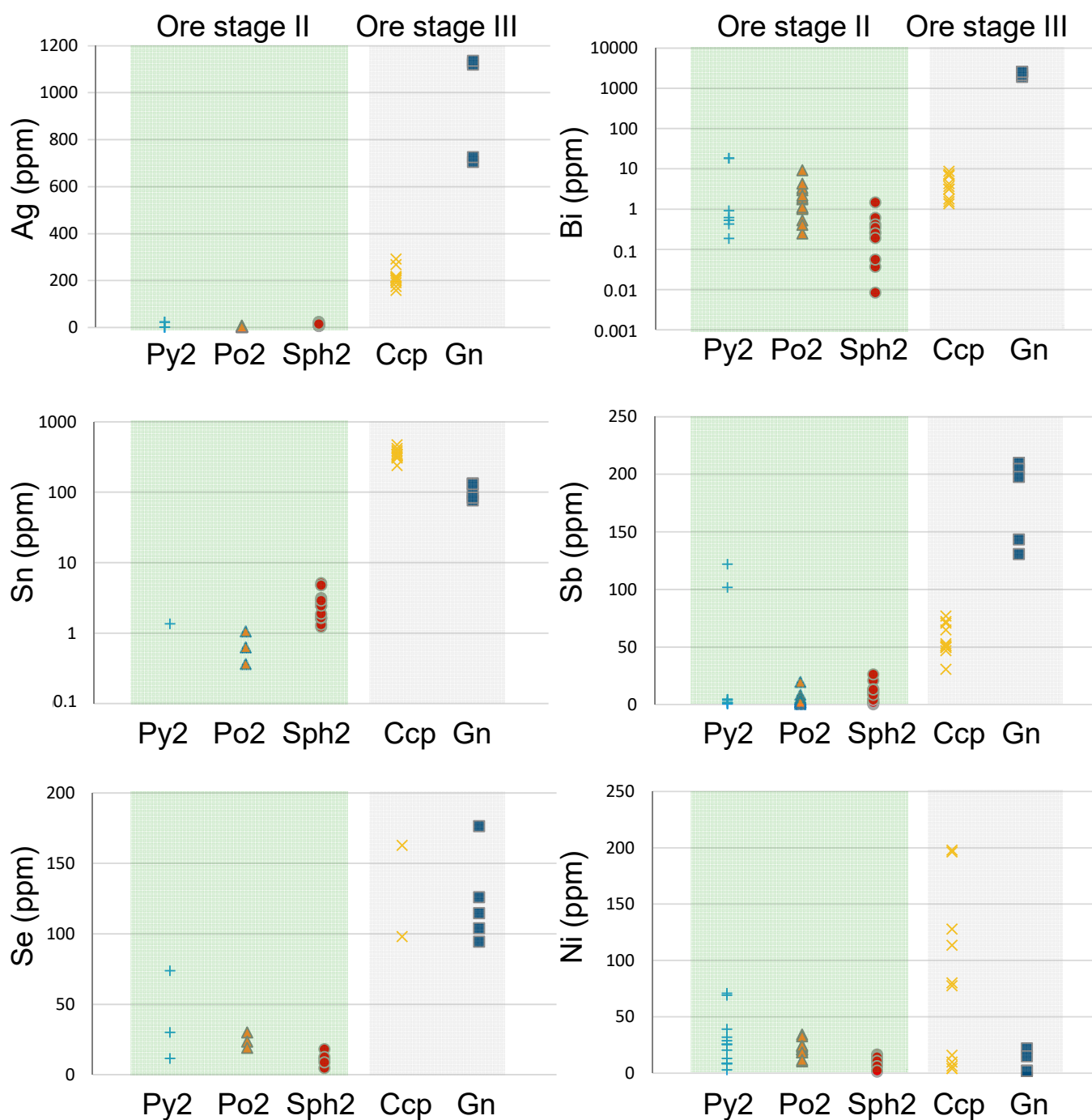


Figure 7. Distribution of main trace elements in major vein sulfides in the Koudiat Aicha deposit (stages II and III). Py2: pyrite 2, Po2: pyrrhotite 2, Sph2: sphalerite 2, Ccp: chalcopyrite, Gn: galena.

6. Fluid Inclusion Studies

Early massive and banded ores are devoid of transparent gangue minerals suitable for microthermometry studies. Both early and late Fe-rich sphalerites are dark in color (nearly opaque), which prevents fluid inclusion studies of these sphalerites. Therefore, in this section we focus on fluid inclusions (FIs) in the second and third (quartz- and carbonate-rich vein) stages. Microthermometry was performed on quartz from pyrrhotite 2 veins—shear zones and in breccia where quartz 1 fragments are commonly recrystallized, acquiring a clear, transparent appearance and crosscut by secondary fluid inclusions assemblages (FIAs) from late ore stages. Calcite in the late veins shows several primary and secondary

FIs suitable for microthermometry studies. In brief, two major types of FIs are present at Koudiat Aïcha: (i) volatile-rich fluid inclusions associated with early ores (quartz 1–pyrite 2–pyrrhotite 2–sphalerite 2–dominated assemblages), referred to as carbonic and aqueous–carbonic FIs, and (ii) aqueous FIs associated with late carbonate vein ores. Notably, the carbonic inclusions are confined to the stage II veins, whereas the aqueous fluid inclusions characterize the stage III veins. Fluid inclusions range in size from a few micrometers to several tens of micrometers (up to 40 μm) and the microthermometric data are summarized in Table 4.

Table 4. Summary of microthermometric data of fluid inclusions from veins (vein stages II and III) at the Koudiat Aïcha deposit. $T_m \text{CO}_2$: melting temperature of the volatile phase; $T_h \text{CO}_2$: homogenization temperature of the volatile phase to the liquid (L), vapor (V) or critical (C) phases; $T_m \text{cl}$: melting temperature of clathrate; T_e : eutectic temperature; $T_m \text{ice}$: melting temperature of ice; T_h : homogenization temperature to the liquid (L) phase; $T_m \text{h}$: melting temperature of halite. All values are in $^\circ\text{C}$, mode: bold font, number of FIs: italic bold font in brackets. See text for fluid inclusion types and comments.

Fluid Inclusions-Vein Ores	Microthermometry Data				
	$T_h \text{CO}_2$	$T_m \text{CO}_2$	$T_m \text{cl}$	$T_m \text{ice}$	T_h
Carbonic/Aqueous carbonic fluids-Ore stage II					
Vc1 random in Q1 (9 FIs)	−149.9/−143.4 (V) −145				
Lw-c FIP in Q1 (15 FIs)			8–11.5	−13.6/−7.6	290–354 > 400 (L)
Lc1 FIP in Q1 (30 FIs)	−141.1/−130.1 (L) −135				
Vc2 - Primary in RecQ/Sphalerite 2 (30 FIs)	−124.6/−96 (V, C, L) −109				
Lc2 FIP in Q1 and recrystallized Q1 (17 FIs)	−60.6/−24.6 (L) −42 and −27	−63.4/−61.6 −62.5			
Aqueous fluids-Ore stage III	T_e	$T_m \text{ice}$	T_h	$T_m \text{h}$	
Lwh (49 FIs) Secondary in Q1 and Q2	−69/−56	−42.6/−30 −35	116–182 (L) 170	143–227 200	
Primary in calcite (8 FIs)			81–114 (L)		
Lw1 (17 FIs) Secondary in quartz Q1, Q2	−56/−53	−28.6/−23.4 −26	117–229 (L) 170		
Lw2 (112 FIs) Secondary in Q1, Q2	−54/−38	−18.2/−2.3 −8	109–261 (L) 160 and 210		
Lw1 (6 FIs) + Lw2 (7 FIs) Secondary/calcite			91–134 (L)		

6.1. Carbonic and Aqueous Carbonic Fluids: Stage II

Inclusions of type Lwc, two-phase aqueous–carbonic FIs (L + V, % liquid H_2O about 70–60%, up to 40 μm in size) with low-density carbonic vapor phase (no carbonic liquid phase observed), are present as random and locally secondary FIAs in quartz 1 microdomains. Inclusions of this Lwc type showed $T_m \text{ice}$ values from -13.6°C to -7.6°C and $T_m \text{clath}$ values between 8°C and 11.5°C (salinity roughly estimated at about 11–17 wt.% NaCl equiv.). Total homogenization occurs exclusively to the liquid phase from 290°C to 354°C for several FIs, while most Lwc inclusions homogenize at $>400^\circ\text{C}$. Lwc FIAs are commonly crosscut by monophasic carbonic inclusions in quartz 1.

Monophasic carbonic FIs (at an ambient temperature of 20°C) are relatively large in size (up to 30 μm) and show several types that can only be distinguished on the basis of low-temperature microthermometric observations. Scarce and irregular vapor FIs (Vc1), randomly distributed in quartz 1 (Figure 8A,B), seem to be earlier than the much more

abundant monophasic liquid FIs of type Lc1. The latter are present mainly as FIAs in dark quartz 1 and recrystallized microdomains (Figure 8C,D) and are commonly associated with pyrrhotite 2, which can even be observed in the same microfractures (Figure 8C). Inclusions of types Vc1 and Lc1 did not allow observation of Tm CO₂. Inclusions of type Vc1 showed Th CO₂ values from $-149.9\text{ }^{\circ}\text{C}$ to $-143.4\text{ }^{\circ}\text{C}$ (mode at $-145\text{ }^{\circ}\text{C}$) to the vapor phase, while Th CO₂ values for Lc1 inclusions ranged from $-141.1\text{ }^{\circ}\text{C}$ to $-130.1\text{ }^{\circ}\text{C}$ (mode at $-135\text{ }^{\circ}\text{C}$) to the liquid phase.

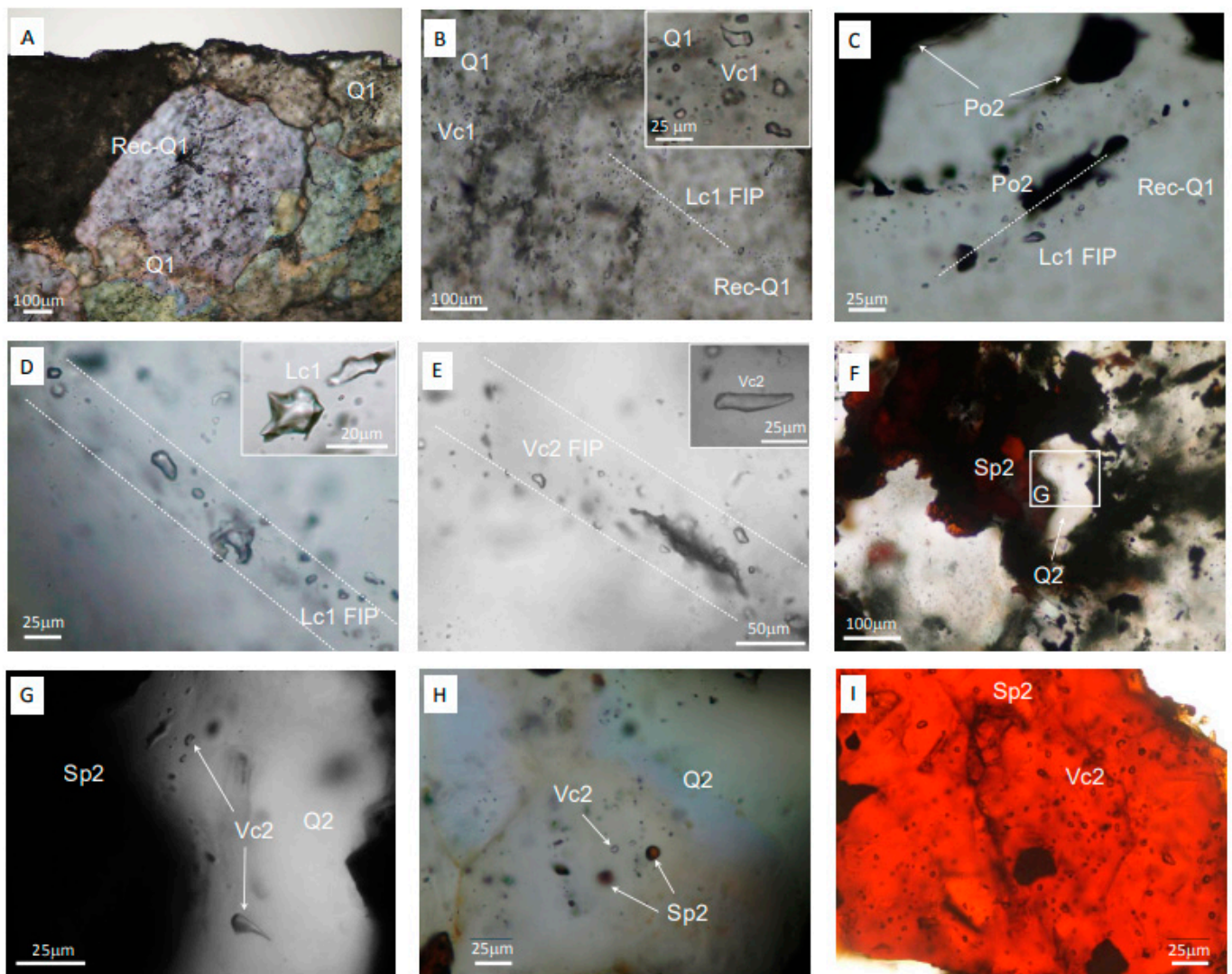


Figure 8. Fluid inclusions from Koudiat Aïcha: early stages. (A) Quartz 1 (Q1) from early veins with dark aspects, due to the abundance of fluid inclusions, and recrystallized microdomains (Rec-Q1). (B) Detail of (A) showing early Vc1 FIs and Lc1 FIs in fluid inclusion planes (FIPs) crosscutting Q1 and recrystallized Q1. (C) Association of pyrrhotite 2 (Po2) with Lc1 FIs in microfractures crosscutting recrystallized Q1 (Rec-Q1). (D) Lc1 FIP in recrystallized Q1. (E) Vc2 FIs in planes crosscutting recrystallized Q1. (F,G) Sphalerite 2 (Sp2) surrounded by quartz 2 (Q2). (H) Association of sphalerite 2 (Sp2) with primary Vc2 fluid inclusions in quartz 2 (Q2). (I) Scattered (primary) Vc2 FIs in sphalerite 2 (Sp2).

Inclusions of type Vc2 are monophasic vapor FIs, regular in shape, and occur as primary inclusions in sphalerite 2 (according to the criteria of [68]) and are scattered in quartz 2 and recrystallized quartz 1 associated with sphalerite 2 (Figure 8E–H). Inclusions of type Vc2 show Th CO₂ values from −124.6 °C to −96 °C (mode at −109 °C) to the vapor phase (rarely to the critical/liquid phase). Monophasic carbonic FIs, probably of type Vc2, are commonly scattered in sphalerite 2 (Figure 8I), the wafers of which are too dark to allow microthermometric observations. Finally, monophasic liquid (or, rarely, vapor) inclusions of type Lc2 are randomly distributed and secondary in FIAs crosscutting recrystallized quartz 1 and show higher T_m CO₂ values from −63.4 °C to −61.6 °C (mode −62.5 °C) and higher Th CO₂ values from −60.6 °C to −24.6 °C to the liquid (two modes at −42 °C and −27 °C) and rarely to the vapor phase.

6.2. Aqueous Fluids, Stage III (Cu Base Metals and Precious Metals)

Inclusions of type Lwh are three-phase aqueous FIs a few micrometers to 40 μm in size, containing, at room temperature, a liquid phase, an up to 20 vol% vapor phase and a halite crystal phase. These inclusions occur as secondary assemblages in quartz from pyrrhotite–sphalerite breccia and veins (Figure 9A,B), where they crosscut assemblages of carbonic and aqueous–carbonic FIs. These Lwh inclusions occur as primary and pseudosecondary assemblages in calcite. Inclusions of type Lwh in quartz show T_e values from −69 °C to −56 °C, T_m ice values between −42.6 °C and −30 °C (mode at −35 °C), Th values from 116 °C to 182 °C (mode at 170 °C) and T_m halite values from 143 °C to 227 °C (mode: 200 °C). Salinity ranges from 34 to 37.7 wt.% equiv. NaCl + CaCl₂ (average 36 wt.% equiv. NaCl + CaCl₂, average NaCl: 19 wt.% equiv., average CaCl₂: 17 wt.% equiv.). In calcite, Lwh FIs show Th values from 81 °C to 114 °C (mode around 100 °C), but T_m halite could not be measured because of the small size of FIs (in general, <10 μm).

Several types of two-phase aqueous FIs (Lw: Liquid plus up to 20 vol% vapor) form regular networks of secondary FIAs crosscutting quartz in breccia and veins (Figure 9C–E) and are also hosted in sphalerite (Figure 9F) as well as calcite crystals. Inclusions of type Lw are also present as scattered FIs and pseudosecondary assemblages in clear quartz microdomains (recrystallized quartz or epitaxial overgrowths) surrounding chalcopyrite–galena ± precious metal assemblages (Figure 9G–J). Two types, Lw1 and Lw2, were distinguished according to their salinities.

Lw1 FIs showed T_e values around −56 °C to −53 °C, T_m ice values from −28.6 °C to −23.4 °C (mode around −26 °C) and Th values from 117 °C to 229 °C (mode at 170 °C). Based on both the first melting temperature and the low ice melting temperature (lower than the eutectic temperature of the H₂O–NaCl system), these are probably calcic brines, and their salinities are estimated to be between 23.2 wt.% NaCl equiv. (eutectic composition of H₂O–NaCl system) and ~30 wt.% NaCl equiv. [61].

Inclusions of type Lw2 show a T_e range from −54 °C to −38 °C, a T_m ice range from −18.2 °C to −2.3 °C, salinity ranges from 3.9 to 21.1 wt.% NaCl equiv. and a Th range from 109 °C to 261 °C (two modes: 160 °C and 200–210 °C).

Aqueous FIs with similar salinities to inclusions of types Lw1 and Lw2 are present as secondary FIAs crosscutting calcite but show lower Th values (91–134 °C, mode at 100 °C), probably due to post-entrapment modifications common in soft minerals, such as carbonates [69–72].

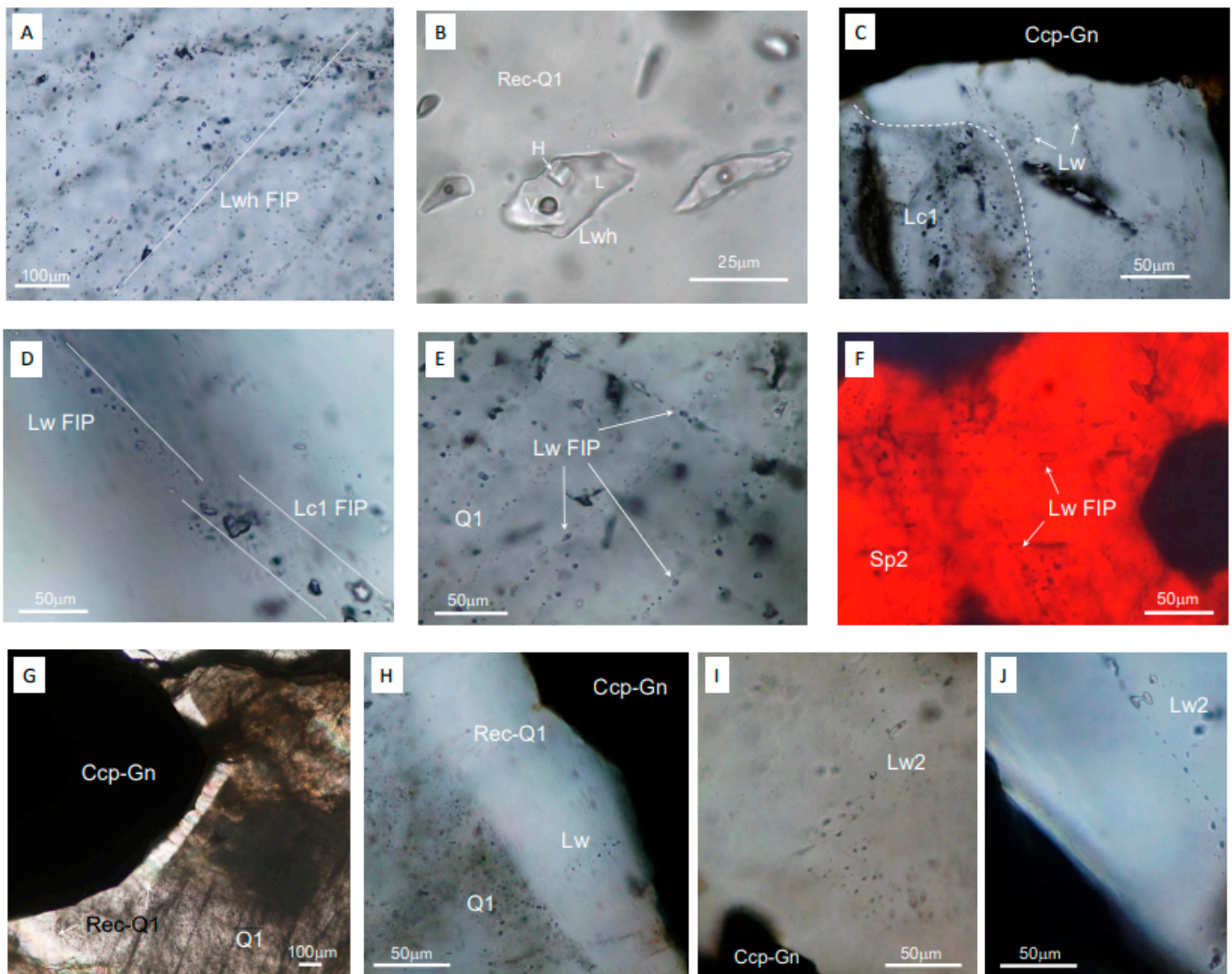


Figure 9. Fluid inclusions from Koudiat Aïcha: late vein stages. (A,B) Lwh FIs in microfractures (fluid inclusion planes (FIPs)) crosscutting quartz 1 from early veins ((B) is a detail of (A)). (C) Lw FIs in recrystallized quartz around chalcopyrite–galena assemblages (Ccp-Gn); Lc1 FIs are exclusively present in early dark quartz. (D) Lw aligned in a reworked early Lc1 FIP crosscutting recrystallized Q1. (E) Lw FIP crosscutting Q1. (F) Lw FIP crosscutting sphalerite 2 (Sp2). (G,H) Chalcopyrite-and-galena (Ccp-Gn)-dominated mineral assemblage (late vein stage) surrounded with recrystallized quartz containing primary Lw FIs. (I,J) Lw2 FIs in clear quartz around chalcopyrite and galena (Ccp-Gn) assemblages.

7. Discussion

As the principal focus of this study is the origin of the quartz and carbonate ore veins at Koudiat Aïcha, this discussion is focused primarily on our results for veins and coeval banded and breccia ores. We also note that the early stratabound massive sulfide ores at Koudiat Aïcha (which have been interpreted as representing VMS-style mineralization) suffered metamorphism and deformation during the Variscan orogeny, and thus their primary features are partly obscured. One key observation worth emphasizing is that the hydrothermal features of the mineralized veins (discussed below) are incompatible with a VMS-type system and instead indicate two subsequent and distinct periods of fluid circulation and upgrading that likely represent an orogenic stage (stage II) followed by a post-orogenic, extensional stage (stage III).

7.1. Early (Quartz) Veins (Stage II)

The stage II veins are dominated by carbonic and aqueous–carbonic fluid inclusions indicative of an orogenic hydrothermal environment, suggesting that the ore-forming fluids were sourced from deeper metamorphic devolatilization. In this context, it is noteworthy that the quartz 1–biotite veins at Koudiat Aïcha show similar mineralogical features and contain similar fluid inclusions (i.e., carbonic vapors, Vc1) to widespread quartz–biotite veins throughout the Central Jebilet, which are considered to be of metamorphic origin [73].

According to our interpretation, high-temperature, moderate-salinity aqueous–carbonic fluids (Th >400 °C, up to 17 wt.% NaCl), represented by inclusions of type Lwc, generated pyrite 2 (prior to deposition of pyrrhotite 2 and sphalerite 2 by carbonic fluids). Similarly, at the Jbel Haïmer vein deposit hosted in the Sarhlef series, aqueous–carbonic FIs with temperature and salinity ranges similar to Lwc inclusions from Kouidia Aïcha are synchronous with pyrite mineralization that crosscuts quartz–biotite veins [22]. Such high-temperature fluids at Kouidiat Aïcha are consistent with temperature estimates obtained in several parts of the Central Jebilet, coeval with HT-LP metamorphism (500–650 °C–200 MPa ± 20 MPa [39,73]).

The pyrrhotite 2–sphalerite 2 assemblage, together with chlorite 2 and white mica (pure muscovite [51]), occurs in veins and shear zones as well as banded and breccia-type ores, and represents the main Zn ore at Kouidiat Aïcha. Textural relationships suggest that pyrrhotite 2 is synchronous with the most abundant carbonic FIs of type Lc1 and that sphalerite 2 is synchronous with Vc2 FIs. Given the close association between sphalerite and pyrrhotite, we used concentrations of Fe, Mn, Ga, In and Ge in sphalerite (EPMA and LA-ICP-MS analysis) to estimate the temperature of this stage [74]. Trace-element-based temperature estimation yielded a range from 280 °C to 330 °C for stage 2 assemblage formation. Notably, Ge and Ga tend to be enriched in low-temperature sphalerite, whereas In is in general enriched in high-temperature sphalerite [64,66,74]. This is in agreement with the relatively high temperature implied by sphalerite 2 that shows Ge levels below or close to the limit of detection and relatively high In contents. Thermometry of coeval chlorite 2 based on the EPMA data (from [51]) also yielded a consistent temperature range of 300–350 °C [75].

Volatile-rich FIs of types Lc1 and Vc2 exhibit very low homogenization temperatures (Th CO₂ values as low as –150 °C); the melting temperatures of the volatile phase (Tm CO₂) could not be observed. Such temperatures are strong evidence that these vapor and liquid FIs are composed predominantly of N₂–CH₄, with lesser amounts of CO₂ [76,77]. Fluid inclusions with similar microthermometric features were also confirmed as N₂–CH₄ fluids by Raman analyses in several parts of the Central Jebilet (in quartz veins crosscutting the Sarhlef series in the Sidi Bou Othmane area [73]; in vein–shear-zone ores from the Kettara massive sulfide–vein deposit [9]; in the Kouidia El Hamra vein deposit [21]; and in the Jbel Haïmer vein deposit [22]; Table 5). Liquid Lc2 FIs show higher Tm CO₂ values (–63.4 to –61.6 °C) closer to those of pure CO₂ (–56.6 °C), indicating that CO₂ is the dominant gas, probably accompanied by other volatiles in lower amounts (i.e., CH₄ and N₂). Fluid inclusions similar to Lc2 are CO₂-dominated, with significant amounts of CH₄ and N₂, described as later than the N₂–CH₄ fluids in the Sarhlef series and in the deposits from the Central Jebilet described above (Table 5, references herein).

The N₂–CH₄–CO₂ ± H₂O fluids that circulated throughout the Central Jebilet were probably sourced from the devolatilization of Sarhlef series rocks during HT-LP metamorphism (>500 °C, about 200 MPa [35,73]). Indeed, water–graphite equilibrium under reducing conditions produces H₂O–CO₂–CH₄-rich fluids [78], while N₂ is released from micas and alkali feldspars during metamorphism [73,79]. The host rocks of Kouidiat Aïcha ores, being mainly metamorphosed graphitic argillites, are thus a likely source of N₂–CH₄–CO₂ ± H₂O metamorphic fluids. Oxygen and hydrogen isotopic data for fluids equilibrated with bulk chlorites in early veins from Kouidiat Aïcha (δ¹⁸O: 6.2 to 9.6; δD: –50 to –41) are consistent with both magmatic and metamorphic fluid domains [51]. However, at Kettara and Roc Blanc deposits ([9,20], respectively), O and H isotope data for early fluids similar to those of Kouidiat Aïcha indicate unambiguously a metamorphic origin.

Table 5. Comparison of microthermometric data for fluid inclusions from early vein stages at Koudiat Aïcha (stage II) with data for C-O-N-H fluid inclusions from metamorphic veins in the Central Jebilet: a: [73]; b: [9]; c: [20]; d: [21]; e: [22]. Raman compositions of volatile phases for carbonic and aqueous–carbonic fluid inclusions in the Central Jebilet are given in mol %; Raman data are not available for Koudiat Aïcha.

Central Jebilet Early Vein–Shear Zone Fluids	Th CO ₂ (°C)	Tm CO ₂ (°C)	N ₂ (mol %)	CH ₄ (mol%)	CO ₂ (mol %)	Kouidiat Aïcha Banded–Veins–Shear Zones Fluids
N ₂ –CH ₄ –(CO ₂) fluids						Early carbonic fluids
Sidi Bou Othmane Metamorphic (a)	–153/–90 L,V,C	–75/–64	50–98	2–35	0–30	Vc1 – Quartz 1 Th CO ₂ : –149.9/–143.4 V
Kettara - Metamorphic (b)	–124.1/–105.2 V (L)		49.8–60.4	39.6–50.2	0	Lc1 – Pyrrhotite 2 Th CO ₂ : –141.1/–130.1 L
Roc Blanc - Metamorphic (c)	–106/–73 V	–85/–71.1	46–47	37–40	14–16	Vc2 – Sphalerite 2 Th CO ₂ : –124.6/–96 V,C,L
Koudia El Hamra (d)	–120/–110 V		58–63	33–38	4–5	
Jbel Haïmer (e)	–71.6/–60.5 V	–102.8/–68.5	39.4–69.8	22.1–51.5	7.7–18.6	
CH ₄ –N ₂ –CO ₂ fluids						
Sidi Bou Othmane	–112/–98 L		23–29	71–75	0	
Kettara	–99.4/–70.4 V,L L		21–38.1	36.1–67.5	11.5–27	
Jbel Haïmer	–97 V	–102	4.8–6.2	64.5–70	23.8–30.7	
CH ₄ Fluid - Kettara	–97.4/–2 L-V			100		
CO ₂ –N ₂ –CH ₄ fluids						Late carbonic fluids Lc2
Sidi Bou Othmane–Central Jebilet	–40/18 L	–68/–57.7	3–30	1–10	60–96	Th CO ₂ : –60.6/–24.6 L Tm CO ₂ : –63.4/–61.6
Kettara		–61.1/–56.7	0–36.1	0–6	57.8–100	
Roc Blanc	–51.8/–29.1 V	–69/–63.7	23–31	18–23	49–58	
Jbel Haïmer	–46.9/18.6 L	–65/–57.6	10.3–29.3	4–12.2	58.5–88	

The role of metamorphic fluid flows along shear zones is also evident at other deposits in the Central Jebilet [8] and elsewhere [80–82]. In some cases, fluxes of metamorphic fluids through pre-existing massive sulfide ores during orogeny have been interpreted to have led to remobilization and upgrading. For example, the Huogeqi Cu–Pb–Zn–Fe deposit [83] and the Kaladawan South Zn–Pb–Cu deposit in China [16], generally considered as SEDEX- and VMS-type deposits, respectively, display similar features to Kouidiat Aïcha. Both deposits show mineralized veins formed by epigenetic flux of metamorphic fluids that crosscut the earlier syngenetic stratiform ores. The Kaladawan South deposit presents a particularly similar geological history to the early history of Kouidiat Aïcha, as massive sulfides (VMS) are coeval with fluids from a magmatic–hydrothermal source while overprinting epigenetic vein ore fluids [84] are metamorphic-derived [16].

7.2. Later (Carbonate) Veins (Stage III)

Fluids associated with stage III (Cu–polymetallic ores) are aqueous fluids (types Lwh and Lw), which occur as secondary inclusions in quartz and unambiguously postdate the N₂–CH₄–(CO₂–H₂O) fluids from stage II. Notably, the Lwh-type inclusions occur as primary inclusions in calcite, whereas the Lw inclusions occur as secondary inclusions in the same calcite, indicating a trend of decreasing salinity over time. Low-salinity FIs (Lw) are scattered or pseudosecondary in clear quartz close to chalcopyrite–galena–sulfosalts intergrowing minerals and are thus considered as synchronous with the deposition of this late assemblage. A gradual decrease in salinity subsequent to the mixing of brines with

very low salinity fluids seems to be at the origin of the successive deposition of chalcopyrite then galena, polymetallic sulfides and sulfosalts, enriched in several trace elements (mainly Ag, Bi, Sb, Sn, Se, Te and Tl), together with precious metal minerals (Ag sulfosalt, Ag-Au alloy and argentite). A low temperature range of 175–210 °C obtained from thermometry of stage III chlorite based on EPMA data (from [51]) is consistent with the average Th range from 160 °C to 210 °C shown by FIs synchronous with later base metal sulfide–precious metal–chlorite 3 vein assemblages.

Similar ore brines are responsible for the deposition of Ag base metal vein deposits from the Central Jebilet (Roc Blanc [20] and Koudia El Hamra [21]; Table 6). Deposition of ore minerals was probably promoted by cooling, dilution (decreasing chlorinity), sulfate reduction by interaction with the graphitic argillite host rock (ores being preferably hosted in black argillite contexts) or some combination thereof. Reduction as a concomitant mechanism for base metal and/or precious metal deposition has been emphasized in several deposits (see [85,86] for the Schwarzwald Ba-F base metal district, SW Germany; [87] for the Copperbelt, DR Congo; [88,89] for the Imiter Ag deposit, Morocco; [20,21], respectively, for the Roc Blanc and Koudia El Hamra Ag deposits, Morocco).

Table 6. Comparison of microthermometric data for ore brines and low-salinity aqueous FIs from late vein stages at Koudiat Aïcha (stage III in bold font) with data for high- to low-salinity aqueous ore fluids from vein deposits in the Central Jebilet: a: Roc Blanc Ag deposit [20]; b: Koudia El Hamra Ag deposit [21]; c: Jbel Haïmer Cu occurrences [22]. Th and Tm h modes in brackets.

Ore Brines-Jebilet Vein Deposits	Salinity wt%	Th (°C)	Tmh (°C)
High salinity brines			
Koudia El Hamra (b)	30–38.1	202–294 (220)	113–246 (200)
Jbel Haïmer (c)	31.3–39	174–264 (220)	155–262 (220)
Koudiat Aïcha	34–37.7	116–182 (170)	143–227 (200)
Intermediate salinity brines			
Roc Blanc (a)	19.6 – >30	139–218 (180)	
Koudia El Hamra (b)	20.3 – > 27	129–283	
Jbel Haïmer (c)	22.4 – >30	186–242	
Koudiat Aïcha	23.2–30	117–229 (170)	
Low salinity aqueous fluids			
Roc Blanc (a)	5.7–19.4	127–244 (180)	
Koudia El Hamra (b)	5.3–20.9	186–298 (230)	
Jbel Haïmer (c)	9–15.3	156–242	
Koudiat Aïcha	3.9–21.1	109–261 (160–210)	

At the scale of Central Jebilet, veins similar to stage III crosscut large swathes of metamorphic quartz–biotite–chlorite veins similar to quartz 1 veins from Koudiat Aïcha. For example, at the Jbel Haïmer Cu deposit, metal-rich brines similar to those from Koudiat Aïcha led to the deposition of ores in carbonate veins crosscutting microdiorite dikes dated at 240 ± 10 Ma [43]. Furthermore, E–W-striking calcite–dolomite veins bearing Pb–Zn–Cu mineralization are known throughout the Central Jebilet as coeval with pre-Atlantic extension (Permian–Triassic) due to the opening of the Central Atlantic (1). Such carbonate veins are associated with brine circulation (Sarhlef, Bramram and Bir N’Has Pb–Zn and Cu deposits [90]).

Considering that these Cu-mineralized veins crosscut igneous rocks throughout the Central Jebilet, we rule out any obvious magmatic source for the causative brines. Instead, all the evidence suggests that the mineralizing brines are probably of basinal origin, the overall salinities and also the low eutectic temperatures (indicative of elevated Ca contents) being consistent with basinal brines. Similar ore brines have been considered as post-Variscan at Jbel Haïmer and interpreted as evaporitic bitters derived from Mesozoic Atlantic sedimentary basins in Morocco [22,23]. Mineralizing brines are thought to have circulated at least at the scale of the Jebilet and are at the origin of other deposits (the Jbel

Ighoud barite deposit, Eastern Jebilet [91]; the Roc Blanc Ag deposit [20]; and the Koudia El Hamra Ag deposit [21]). Thermal and tectonic stages coeval with the Central Atlantic rifting constitute the main periods for brine migration in each of these locations. Deep circulation of evaporitic brines into basement rocks also yielded a variety of base-metal-bearing veins in other extensional settings, such as in the Rheingraben [85,86,92,93]. Similarly, we surmise that ductile–brittle Variscan shear zones and fractures were reactivated as normal faults during post-Variscan deformation events [50,94–96], in addition to the E–W pre-Atlas extension faults, enabling the circulation of post-Variscan sedimentary brines and low-salinity aqueous fluids to form the stage III veins.

Successive pulses of distinct hydrothermal fluids, commonly suggested as a causative mechanism in the formation of telescoped polyphase mineralization, are well-known in several sulfide ore deposits in Morocco. Panafrican to Variscan magmatic and/or metamorphic ores followed by later sedimentary brine circulation and base metal–precious metal deposition during the Mesozoic are typical features of most Anti-Atlas deposits, including the Zgounder (Ag–Hg), Bou Azzer (Co–Ni–Ag–Au) and Imiter (Ag–Hg) deposits [97–100] and the Jebilet deposits (Roc Blanc, Koudia El Hamra and Jbel Haïmer). In base metal–precious metal–fluorite–barite vein deposits, reactivated faults hosted Paleozoic and Mesozoic mineralization in the Erzgebirge and Schwarzwald vein deposits coeval with sedimentary brines related to continental rifting [93,101–103].

7.3. Koudiat Aïcha Vein Ores in Their Regional Massive Sulfide Context

The Koudiat Aïcha deposit exhibits similar features to the Draa Sfar deposit, particularly the Sidi Mbarek Cu-rich lenses that constitute the northern part of the deposit. Outigua et al. [11] emphasized that the stratiform orebodies are pyrrhotite-rich, whereas chalcopyrite-rich quartz veins are structurally controlled and associated with shear zones. The early pyrrhotite-dominated mineralization at Draa Sfar is thought to have been remobilized in reactivated shear zones, leading to deposition of the chalcopyrite-rich mineral assemblage [11]. This model is expanded to the major massive sulfide orebodies in Central Jebilet present as subvertical lenses deformed and remobilized into shear-zone-hosted lenses [10]. N'Diaye et al. [9] suggested that the Kettara sulfide deposit was related to syn-metamorphic fluid migration through shear zones. In the Kettara and Koudiat Aïcha massive sulfide deposits, contributions of magmatic, metamorphic and basinal waters in hydrothermal fluids may be supported by the mixed O–H isotope data [10].

Moreover, the lead isotopic signature suggested that two types of hydrothermal fluids were involved in the Draa Sfar deposit: early Zn-rich and later Cu-rich fluids [5]. This is in general agreement with our results concerning Koudiat Aïcha, where the succession of polyphase Zn-dominated ores followed by Cu-dominated veins reflects a change in fluid type and source (i.e., Variscan metamorphic fluids, likely followed later by basinal brines). Copper–lead–precious metal ores represent a vein stage that postdates the early massive ores and major Zn ores and postdates the Variscan magmatic–metamorphic events, instead representing the deep circulation of evaporitic brines during post-orogenic extension.

8. Conclusions

The results of the present study indicate that sulfide–quartz veins and banded and breccia sulfide ores, with abundant pyrrhotite, pyrite and sphalerite, in the Koudiat Aïcha deposit are related to N_2 – CH_4 –(CO_2 – H_2O) fluids. These fluids were derived from metamorphic devolatilization of the host volcanosedimentary and sedimentary rocks during the Variscan orogeny. Late brine circulation led to the deposition of Cu–Pb–(\pm Ag \pm Au) minerals in carbonate veins that crosscut the pre-existing massive, banded and early quartz vein ores. Early quartz veins underwent reworking during brine circulation and late carbonate-ore mineral deposition. The late saline fluids most likely correspond to reported large-scale, post-Variscan circulation of evaporitic brine in the Jebilet massif during the extensional regime associated with the Central Atlantic opening. Our results thus show that the

Koudiat Aïcha deposit was the result of superimposed ore-forming processes in different environments, each of which contributed to the ultimate endowment of this deposit.

Author Contributions: Conceptualization, S.E.; methodology, S.E. and B.Z.; validation, S.E., B.Z., A.K. and A.O.; formal analysis, S.E. and B.Z.; investigation, S.E., B.Z., M.F.; resources, S.E. and B.Z.; data curation, S.E., B.Z. and M.F.; writing—original draft preparation, S.E. and B.Z.; writing—review and editing, S.E., B.Z. and M.S.-M.; supervision, S.E.; funding acquisition, S.E. and B.Z. All authors have read and agreed to the published version of the manuscript.

Funding: This research received no external funding.

Acknowledgments: Basem Zoheir acknowledges the Alexander von Humboldt Foundation for supporting his research stay at Kiel University. Max Frenzel is thanked for his help with sphalerite temperature calculations. Abdelwahab Knidiri is acknowledged for sample preparation and Rachid El Moutamanni (SEM-CAC Cadi Ayyad University) for help with SEM analyses. We thank three anonymous reviewers for their comments that helped us to improve the original manuscript and Astrid Yang for editorial handling.

Conflicts of Interest: The authors declare no conflict of interest.

References

1. Huvelin, P. Etude géologique et gîtologique du massif hercynien des Jebilet (Maroc occidental). *Notes Mémoires Service Géologique Maroc* **1977**, *232*, 308.
2. Bernard, A.J.; Maier, O.W. Mellal. Aperçu sur les amas sulfurés massifs des hercynides marocaines. *Miner. Depos.* **1988**, *23*, 104–114. [[CrossRef](#)]
3. Hibti, M. Les amas Sulfurés des Guemassa et des Jebilet (Meseta Sud-Occidentale, Maroc): Temoins de L’hydrothermalisme Précoce dans le Bassin Mesetien. Ph.D. Thesis, Cadi Ayyad University, Marrakesh, Morocco, 2001; 301p.
4. Belkabir, A.; Gibson, H.L.; Marcoux, E.; Lentz, D.; Rziki, S. Geology and wall rock alteration at the Hercynian Draa Sfar Zn–Pb–Cu massive sulphide deposit, Morocco. *Ore Geol. Rev.* **2008**, *33*, 280–306. [[CrossRef](#)]
5. Marcoux, E.; Belkabir, A.; Gibson, H.L.; Lentz, D.; Ruffet, G. Draa Sfar, Morocco: A Visean (331 Ma) pyrrhotite-rich, polymetallic volcanogenic massive sulphide deposit in a Hercynian sediment-dominant terrane. *Ore Geol. Rev.* **2008**, *33*, 307–328. [[CrossRef](#)]
6. Moreno, C.; Sáez, R.; González, F.; Almodóvar, G.; Toscano, M.; Playford, G.; Alansari, A.; Rziki, S.; Bajddi, A. Age and depositional environment of the Draa Sfar massive sulphide deposit, Morocco. *Miner. Depos.* **2008**, *43*, 891–911. [[CrossRef](#)]
7. Ben Aïssi, L. Contribution à l’étude gîtologique des amas sulfurés polymétalliques de Draa Sfar et de Koudiat Aïcha: Comparaison avec les gisements de Ben Sliman et de Kettara (Jebilet centrales, Maroc hercynien). Unpublished. Ph.D. Thesis, Cadi Ayyad University, Marrakesh, Morocco, 2008; 353p.
8. Essaifi, A.; Hibti, M. The hydrothermal system of Central Jebilet (Variscan Belt, Morocco): A genetic association between bimodal plutonism and massive sulphide deposits? *J. Afr. Earth Sci.* **2008**, *50*, 188–203. [[CrossRef](#)]
9. N’Diaye, I.; Essaifi, A.; Dubois, M.; Lacroix, B.; Goodenough, K.M.; Maacha, L. Fluid flow and polymetallic sulfide mineralization in the Kettara shear zone (Jebilet Massif, Variscan Belt, Morocco). *J. Afr. Earth Sci.* **2016**, *119*, 17–37. [[CrossRef](#)]
10. Essaifi, A.; Goodenough, K.; Tornos, F.; Outigua, A.; Ouadjou, A.; Maacha. The Moroccan Massive Sulphide Deposits: Evidence for a Polyphase Mineralization. *Minerals* **2019**, *9*, 156. [[CrossRef](#)]
11. Outigua, A.; Essaifi, A.; Corsini, M.; Outhounjite, M.; Zouhair, M. Sidi M’Barek: A representative example of the Moroccan massive sulphide deposits. *Geol. Soc. Lond. Spec. Publ.* **2021**, *502*, 67–95. [[CrossRef](#)]
12. Admou, S.; Branquet, Y.; Badra, L.; Barbanson, L.; Outhounjite, M.; Khalifa, A.; Zouhair, M.; Maacha, L. The Hajjar Regional Transpressive Shear Zone (Guemassa Massif, Morocco): Consequences on the deformation of the Base-Metal Massive Sulfide Ore. *Minerals* **2018**, *8*, 435. [[CrossRef](#)]
13. Castroviejo, R.; Quesada, C.; Soler, M. Post-depositional tectonic modification of VMS deposits in Iberia and its economic significance. *Miner. Depos.* **2011**, *46*, 615–637. [[CrossRef](#)]
14. Chauvet, A. Structural Control of Ore Deposits: The Role of Pre-existing Structures on the Formation of Mineralised Vein Systems. *Minerals* **2019**, *9*, 56.
15. Kampmann, T.; Jansson, N.F.; Stephens, M.B.; Olin, P.H.; Gilbert, S.; Wanhainen, C. Syn-tectonic sulphide remobilization and trace element redistribution at the Falun pyritic Zn–Pb–Cu–(Au–Ag) sulphide deposit, Bergslagen, Sweden. *Ore Geol. Rev.* **2018**, *96*, 48–71. [[CrossRef](#)]
16. Wang, C.; Zheng, Y.; Yu, P. Ore genesis and fluid evolution of the Kaladawan South Zn–Pb–Cu ore field, eastern Altyn Mountains (NW China): Evidence from fluid inclusions, H–O isotopes and geochronology. *Ore Geol. Rev.* **2018**, *102*, 300–312. [[CrossRef](#)]
17. Lotfi, F.; Belkabir, A.; Brown, A.C.; Marcoux, E.; Brunet, S.; Maacha, L. Geology and Mineralogy of the Hercynian Koudiat Aïcha Polymetallic (Zn–Pb–Cu) Massive Sulphide Deposit, Central Jebilet, Morocco. *Explor. Min. Geol.* **2008**, *17*, 145–162. [[CrossRef](#)]

18. Chauvet, A.; Onézime, J.; Charvet, J.; Barbanson, L.; Faure, M. Syn- to late-tectonic stockwork emplacement within the Spanish section of the Iberian Pyrite Belt: Structural, textural and mineralogical constraints in the Tharsis-La Zarza areas. *Econ. Geol.* **2004**, *99*, 1781–1792. [[CrossRef](#)]
19. Chauvet, A. Editorial for Special Issue “Structural Control of Mineral Deposits: Theory and Reality”. *Minerals* **2019**, *9*, 171. [[CrossRef](#)]
20. Essarraj, S.; Boiron, M.C.; Cathelineau, M.; Tarantola, A.; Leisen, M.; Hibti, M. Mineralogy and ore fluid chemistry of the Roc Blanc Ag deposit, Jebilet Variscan massif, Morocco. *J. Afr. Earth Sci.* **2017**, *127*, 175–193. [[CrossRef](#)]
21. Nshimiyimana, F.; Essarraj, S.; Hibti, M.; Boulvais, P.; Boyce, A.J.; Marignac, C.; Maacha, L. The Koudia El Hamra Ag–Pb–Zn deposit, Jebilet, Morocco: Mineralogy and ore fluid characterization. *J. Afr. Earth Sci.* **2018**, *145*, 1–17. [[CrossRef](#)]
22. Essarraj, S.; Boiron, M.C.; Cathelineau, M.; Peiffert, C. Evaporitic brines and copper-sulfide ore at Jbel Haïmer (Central Jebilet, Morocco). *Ore Geol. Rev.* **2021**, *129*, 103920. [[CrossRef](#)]
23. Essarraj, S.; Boiron, M.C.; Cathelineau, M.; Peiffert, C. Evaporitic brines and copper-sulfide ore at Jbel Haïmer (Central Jebilet, Morocco): A reply. *Ore Geol. Rev.* **2021**, *140*, 104409. [[CrossRef](#)]
24. Lagarde, J.L.; Choukroune, P. Cisaillement ductile et granitoïdes syntectoniques: L'exemple du massif hercynien des Jebilet (Maroc). *Bull. Société Géologique De Fr.* **1982**, *24*, 299–307. [[CrossRef](#)]
25. Le Corre, C.; Bouloton, J. Un modèle de “structure en fleur” associant décrochement et convergence: Les Jebilet centro-occidentales (Maroc hercynien). *Comptes Rendus Académie Sci. Paris* **1987**, *13*, 751–755.
26. Aarab, E.; Beauchamp, J. Le magmatisme carbonifère préorogénique des Jebilet centrales (Maroc). Précisions pétrographiques et sédimentaires. Implications géodynamiques. *Comptes Rendus Académie Sci. Paris* **1987**, *304*, 169–175.
27. Beauchamp, J. Le Carbonifère inférieur des Jebilet et de l'Atlas de Marrakech (Maroc): Migration et comblement d'un bassin marin. *Bull. Société Géologique De Fr.* **1984**, *7*, 1025–1032. [[CrossRef](#)]
28. Beauchamp, J.; Izart, A.; Piqué, A. Les bassins d'avant-pays de la chaîne hercynienne au Carbonifère inférieur. *Can. J. Earth Sci.* **1991**, *28*, 2024–2041. [[CrossRef](#)]
29. Huvelin, P. Sur l'âge viséen supérieur des schistes de Kettara et du Jbel Sarhlef (Jebilet centrales, Maroc). *Comptes Rendus Somm. Société Géologique De Fr.* **1961**, 290–291.
30. Bordonaro, M. Tectonique et pétrographie du district à pyrrhotite de Kettara (Paléozoïque des Jebilet, Maroc). Unpublished. Ph.D. Thesis, Louis Pasteur University, Strasbourg, France, 1983; 132p.
31. Essaifi, A.; Samson, S.; Goodenough, K. Geochemical and Sr–Nd isotopic constraints on the petrogenesis and geodynamic significance of the Jebilet magmatism (Variscan Belt, Morocco). *Geol. Mag.* **2013**, *151*, 666–691. [[CrossRef](#)]
32. Essaifi, A.; Potrel, A.; Capdevila, R.; Lagarde, J.L. U–Pb dating: Emplacement age of the bimodal magmatism of Central Jebilet (Variscan Belt, Morocco). Geodynamic implications. *Comptes Rendus Geosci.* **2003**, *335*, 193–203. [[CrossRef](#)]
33. Essaifi, A.; Lagarde, J.L.; Capdevila, R. Deformation and displacement from shear zone patterns in the Variscan upper crust, Jebilet, Morocco. *J. Afr. Earth Sci.* **2001**, *32*, 335–350. [[CrossRef](#)]
34. Mrini, Z.; Rafi, A.; Duthou, J.L.; Vidal, P. Chronologie Rb–Sr des granitoïdes hercyniens du Maroc: Conséquences. *Bull. Société Géologique De Fr.* **1992**, *163*, 281–291.
35. Delchini, S.; Lahfid, A.; Lacroix, B.; Baudin, T.; Hoepffner, C.; Guerrot, C.; Lach, P.; Saddiqi, O.; Ramboz, C. The geological evolution of the Variscan Jebilet massif, Morocco, inferred from new structural and geochronological analyses. *Tectonics* **2018**, *37*, 4470–4493. [[CrossRef](#)]
36. El Hassani, A. Etude lithostratigraphique, tectonique et pétrographique de la région de Sidi Bou-Othmane (Maroc). Contribution à la connaissance de l'évolution du segment hercynien des Jebilet centrales. Unpublished. Ph.D. Thesis, University of Aix-Marseille, Marseille, France, 1980; 114p.
37. Bouloton, J. Mise en évidence de cordiérite héritée des terrains traversés dans le pluton granitique des Oulad Ouaslam (Jebilet, Maroc). *Can. J. Earth Sci.* **1992**, *29*, 658–668. [[CrossRef](#)]
38. Tisserant, D. Les isotopes du strontium et l'histoire hercynienne du Maroc. Etude de quelques massifs atlasiques et m'és'etiens. Unpublished. Ph.D. Thesis, University of Strasbourg, Strasbourg, France, 1977; 103p.
39. Delchini, S.; Lahfid, A.; Plunder, A.; Michard, A. Applicability of the RSCM geothermometry approach in a complex tectono-metamorphic context: The Jebilet massif case study (Variscan Belt, Morocco). *Lithos* **2016**, *256–257*, 1–12. [[CrossRef](#)]
40. Gasquet, D.; Bouloton, J. *Les Filons de Microdiorite des Jebilet Centrales (Meseta Marocaine): Pré-Rifting Permien? Réunion extraordinaire SGF: Marrakech, Morocco, 1995*; p. 55.
41. Youbi, N.; Bellon, H.; Marzin, A.; Piqué, A.; Cotten, J.; Cabanis, B. Du cycle orogénique hercynien au pré-rifting de l'Atlantique central au Maroc occidental: Les microdiorites des Jbilet sont-elles des marqueurs magmatiques de ce passage? *Comptes Rendus Académie Sci. Paris* **2001**, *333*, 295–302. [[CrossRef](#)]
42. Dostal, J.; Keppie, J.D.; Hamilton, M.A.; Aarab, E.M.; Lefort, J.P.; Murphy, J.B. Crustal xenoliths in Triassic lamprophyre dykes in western Morocco: Tectonic implications for the Rheic ocean suture. *Geol. Mag.* **2005**, *142*, 159–172. [[CrossRef](#)]
43. Bouloton, J.; Gasquet, D.; Pin, C. Petrogenesis of the Early-Triassic quartz-monzodiorite dykes from Central Jebilet (Moroccan Meseta): Trace element and Nd–Sr isotope constraints on magma sources, and inferences on their geodynamic context. *J. Afr. Earth Sci.* **2019**, *149*, 451–464. [[CrossRef](#)]
44. Bouloton, J.; Gasquet, D. Melting and undercooled crystallization of felsic xenoliths from minor intrusions (Jebilet massif, Morocco). *Lithos* **1995**, *35*, 201–219. [[CrossRef](#)]

45. Tourani, A.; Lund, J.J.; Banaouiss, N.; Gaupp, R. Stratigraphy of Triassic syn-rift deposits in western Morocco. *Zent. Geol. Palaeontol.* **2000**, *9*, 1193–1215.
46. Medina, F. Superimposed extensional tectonics in the Argana Triassic formations (Morocco), related to the early rifting of the Central Atlantic. *Geol. Mag.* **1991**, *128*, 525–536. [[CrossRef](#)]
47. El Arabi, E.H. La série permienne et triasique du rift haut-atlasique: Nouvelles datations; évolution tectonosédimentaire. Unpublished. Ph.D. Thesis, Hassan II University, Casablanca, Morocco, 2007; 225p.
48. Studer, M.A. Tectonique et pétrographie des roches sédimentaires, éruptives et métamorphiques de la région de Tounfite-Tirrhist (Haut Atlas central mésozoïque, Maroc). *Notes Mémoires Ser. Géologique Maroc* **1987**, *43*, 65–197.
49. Saddiqi, O.; El Haïmer, F.; Michard, A.; Barbarand, J.; Ruiz, G.M.H.; Mansour, E.M.; Leturmy, P.; Frizon de Lamotte, D. Apatite fission-track analyses on basement granites from south-western Meseta, Morocco: Paleogeographic implications and interpretation of AFT age discrepancies. *Tectonophysics* **2009**, *475*, 29–37. [[CrossRef](#)]
50. Frizon de Lamotte, D.; Zizi, M.; Missenard, Y.; Hafid, M.; El Azzouzi, M.; Charrière, A.; Maury, R.C.; Taki, Z.; Benammi, M.; Michard, A. The Atlas system. In *Continental Evolution: The Geology of Morocco*; Michard, A., Saddiqi, O., Chalouan, A., Frizon de Lamotte, D., Eds.; Springer: Heidelberg, Germany, 2008; pp. 133–202.
51. Lotfi, F.; Belkabar, A.; Brunet, S.; Brown, A.C.; Marcoux, E. Lithochemical, mineralogical analyses and oxygen–hydrogen isotopes of the Hercynian Koudiat Aïcha massive sulphide deposit, Morocco. *J. Afr. Earth Sci.* **2010**, *56*, 150–166. [[CrossRef](#)]
52. Fietzke, J.; Frische, M. Experimental evaluation of elemental behavior during LA-ICP-MS: Influences of plasma conditions and limits of plasma robustness. *J. Anal. At. Spectrom.* **2016**, *31*, 234–244. [[CrossRef](#)]
53. Wolf, R.E.; Wilson, S.A. USGS Reference Materials Program: U.S. Geological Survey Fact Sheet-3056. 2007; p. 4. Available online: http://minerals.cr.usgs.gov/geo_chem_stand/ (accessed on 10 October 2022).
54. Wilson, S.A.; Ridley, W.I.; Koenig, A.E. Development of sulfide calibration standards for the laser ablation inductively-coupled plasma mass spectrometry technique. *J. Anal. At. Spectrom.* **2002**, *17*, 406–409. [[CrossRef](#)]
55. Wohlgemuth-Ueberwasser, C.C.; Ballhaus, C.; Berndt, J.; Stotternée Paliulionyte, V.; Meisel, T. Synthesis of PGE sulfide standards for laser ablation inductively coupled plasma mass spectrometry (LA-ICP-MS). *Contrib. Mineral. Petrol.* **2007**, *154*, 607–617. [[CrossRef](#)]
56. Wise, S.A.; Watters, R.L. *Certificate of Analysis Standard Reference Material 616*; National Institute of Standards and Technology: Gaithersburg, MD, USA, 2012.
57. Fietzke, J.; Liebetrau, V.; Günther, D.; Gürs, K.; Hametner, K.; Zumholz, K.; Hansteen, T.H.; Eisenhauer, A. An alternative data acquisition and evaluation strategy for improved isotope ratio precision using LA-MC-ICP-MS applied to stable and radiogenic strontium isotopes in carbonates. *J. Anal. At. Spectrom.* **2008**, *23*, 955–961. [[CrossRef](#)]
58. Boiron, M.C.; Essarraj, S.; Sellier, E.; Cathelineau, M.; Lespinasse, M.; Poty, B. Identification of fluid inclusions in relation to their host microstructural domains in quartz by cathodoluminescence. *Geochim. Cosmochim. Acta* **1992**, *56*, 175–185. [[CrossRef](#)]
59. Shepherd, T.J. Temperature-programmable heating-freezing stage for microthermometric analysis of fluid inclusion. *Econ. Geol.* **1981**, *76*, 1244–1247. [[CrossRef](#)]
60. Roedder, E. Fluid Inclusions. *Rev. Mineral.* **1984**, *12*, 644. [[CrossRef](#)]
61. Bodnar, R.J.; Vityk, M.O. Interpretation of microthermometric data for H₂O-NaCl fluid inclusions. In *Fluid Inclusions in Minerals, Methods and Applications*; De Vivo, B., Frezzotti, M.L., Eds.; Virginia Tech: Blacksburg, VA, USA, 1994; pp. 117–130.
62. Steele-MacInnis, M.; Bodnar, R.J.; Naden, J. Numerical model to determine the composition of H₂O-NaCl-CaCl₂ fluid inclusions based on microthermometric and microanalytical data. *Geochim. Cosmochim. Acta* **2011**, *75*, 21–40. [[CrossRef](#)]
63. Schwarz, E.J.; Vaughan, D.J. Magnetic phase relations of pyrrhotite. *J. Geomagn. Geoelectr.* **1972**, *24*, 441–458. [[CrossRef](#)]
64. Cook, N.J.; Ciobanu, C.L.; Pring, A.; Skinner, W.; Shimizu, M.; Danyushevsky, L.; Saini-Eidukat, B.; Melcher, F. Trace and minor elements in sphalerite: A LA-ICPMS study. *Geochim. Cosmochim. Acta* **2009**, *73*, 4761–4791. [[CrossRef](#)]
65. Bowles, J.F.W.; Howie, R.A.; Vaugnan, D.J.; Zussman, J. *Rock-Forming Minerals 5A, Non-Silicates: Oxides, Hydroxides, and Sulfides*, 2nd ed.; The Geological Society of London: London, UK, 2011; 920p.
66. Belissant, R.; Boiron, M.C.; Luais, B.; Cathelineau, M. LA-ICP-MS analyses of minor and trace elements and bulk Geisotopes in zoned Ge-rich sphalerites from the Noailhac—Saint- Salvy deposit (France): Insights into incorporation mechanisms and ore deposition processes. *Geochim. Cosmochim. Acta* **2014**, *126*, 518–540. [[CrossRef](#)]
67. Cook, N.J.; Ciobanu, C.L.; Brugger, J.; Etschmann, B.; Howard, D.L.; de Jonge, M.D.; Ryan, C.; Paterson, D. Determination of the oxidation state of Cu in substituted Cu-In-Fe-bearing sphalerite via μ -XANES spectroscopy. *Am. Mineral.* **2012**, *97*, 476–479. [[CrossRef](#)]
68. Wilkinson, J.J. Fluid inclusions in hydrothermal ore deposits. *Lithos* **2001**, *55*, 229–272. [[CrossRef](#)]
69. Larson, L.T.; Miller, J.D.; Nadeau, J.E.; Roedder, E. Two sources of error in low-temperature inclusion homogenization determination, and corrections on published temperatures for the East Tennessee and Laisvall deposits. *Econ. Geol.* **1973**, *68*, 113–116. [[CrossRef](#)]
70. Bodnar, R.J.; Bethke, P.M. Systematics of stretching of fluid inclusions I: Fluorite and sphalerite at 1 atmosphere confining pressure. *Econ. Geol.* **1984**, *79*, 141–161. [[CrossRef](#)]
71. Ulrich, M.R.; Bodnar, R.J. Systematics of stretching of fluid inclusions. II. Barite at 1 atm confining pressure. *Econ. Geol.* **1988**, *83*, 1037–1046. [[CrossRef](#)]

72. Goldstein, R.H.; Reynolds, T.J. *Systematics of Fluid Inclusions in Diagenetic Minerals*; Short Course 31; Society of Economic Paleontologists and Mineralogists: Tulsa, OK, USA, 1994; 199p. [[CrossRef](#)]
73. Bastoul, A. Origine et évolution des Fluides Hydro-Carbo-Azotés dans les Formations Métamorphiques: Relations avec les Minéralisations Associées (U, Au, graphite). Unpublished. Ph.D. Thesis, Nancy I University, Nancy, France, 1992; 311p.
74. Frenzel, M.; Hirsch, T.; Gutzmer, J. Gallium, germanium, indium, and other minor and trace elements in sphalerite as a function of deposit type—A meta-analysis. *Ore Geol. Rev.* **2016**, *76*, 52–78. [[CrossRef](#)]
75. Bourdelle, F.; Cathelineau, M. Low- Temperature chlorite geothermometry: A graphical representation based on a T-R²⁺-Si diagram. *Eur. J. Mineral.* **2015**, *27*, 617–626. [[CrossRef](#)]
76. Hollister, L.S.; Burruss, R.C. Phase equilibria in fluid inclusions from the Khtada Lake metamorphic complex. *Geochim. Cosmochim. Acta* **1976**, *40*, 163–175. [[CrossRef](#)]
77. Touret, J. An empirical phase diagram for a part of N₂-CO₂ system at low temperatures. *Chem. Geol.* **1982**, *37*, 49–58. [[CrossRef](#)]
78. Huff, T.A.; Nabelek, P.I. Production of carbonic fluids during metamorphism of graphitic pelites in a collisional orogeny. An assessment from fluid inclusions. *Geochim. Cosmochim. Acta* **2007**, *71*, 4997–5015. [[CrossRef](#)]
79. Wright, A.J.; Blamey, N.J.F.; Conliffe, J.; Costanzo, A.; Parnell, J. Origin of vein-graphite derived from metamorphic fluids in Moine (Glenfinnan Group) rocks NW Scotland. *Scott. J. Geol.* **2012**, *48*, 47–59. [[CrossRef](#)]
80. Lebedev, V.I.; Nagaytsev, Y.V. Minor elements in metamorphic rocks as an ore-metal source for certain deposits. *Geochem. Int.* **1980**, *17*, 31–39.
81. Haack, U.; Heinrichs, H.; Boness, M.; Schneider, A. Loss of metals from pelites during regional metamorphism. *Contrib. Mineral. Petrol.* **1984**, *85*, 116–132. [[CrossRef](#)]
82. Hammerli, J.; Spandler, C.; Oliver, N.H.S.; Sossi, P.; Dipple, G.M. Zn and Pb mobility during metamorphism of sedimentary rocks and potential implications for some base metal deposits. *Miner. Depos.* **2015**, *50*, 657–664. [[CrossRef](#)]
83. Zhong, R.; Li, W.; Chen, Y.; Huo, H. Ore-forming conditions and genesis of the Huogeqi Cu–Pb–Zn–Fe deposit in the northern margin of the North China Craton: Evidence from ore, petrologic characteristics. *Ore Geol. Rev.* **2012**, *44*, 107–120. [[CrossRef](#)]
84. Liu, B.; Cao, F.G.; Liu, W.G.; Lei, H.M.; Liu, M.F. Geological feature and metallogenic conditions analysis of Kaladawanxi Pb-Zn ore deposit in the Altyn area. *Xinjiang Geol.* **2012**, *30*, 55–58, (In Chinese, with English abstract).
85. Walter, B.F.; Burisch, M.; Fusswinkel, T.; Marks, M.A.W.; Steele-MacInnis, M.; Wälle, M.; Apukhtina, O.; Markl, G. Multi-reservoir fluid mixing processes in rift-related hydrothermal veins, Schwarzwald, SW-Germany. *J. Geochem. Explor.* **2018**, *186*, 158–186. [[CrossRef](#)]
86. Walter, B.F.; Kortenbruck, P.; Scharrer, M.; Zeitvogel, C.; Wälle, M.; Mertz-Kraus, R.; Markl, G. Chemical evolution of ore-forming brines—Basement leaching, metal provenance, and the redox link between barren and ore-bearing hydrothermal veins. A case study from the Schwarzwald mining district in SW-Germany. *Chem. Geol.* **2019**, *506*, 126–148. [[CrossRef](#)]
87. Heijlen, W.; Banks, D.A.; Muchez, P.; Stensgard, B.M.; Yardley, B. The Nature of Mineralizing Fluids of the Kipushi Zn-Cu Deposit, Katanga, Democratic Republic of Congo: Quantitative Fluid Inclusion Analysis using Laser Ablation ICP-MS and Bulk Crush-Leach Methods. *Econ. Geol.* **2008**, *103*, 1459–1482. [[CrossRef](#)]
88. Pasava, J. Geochemistry and role of anoxic sediments in the origin of the Imiter deposit in Morocco. *Czech Geol. Surv. Bull.* **1994**, *69*, 1–11.
89. Borisenko, A.S.; Lebedev, V.I.; Borovikov, A.A.; Pavlova, G.G.; Kalinin, Y.A.; Nevol'ko, P.A.; Maacha, L.; Kostin, A.V. Forming conditions and age of native silver deposits in Anti-Atlas (Morocco). *Dokl. Earth Sci.* **2014**, *456*, 663–666. [[CrossRef](#)]
90. Nshimiyimana, F.; Essarraj, S.; Hibti, M.; Boulvais, Ph.; Boyce, J.A. Post-Hercynian circulation of brines in the central Jebilet: The Bir N'has, Sarhlef and Bramram Pb-Zn deposits, Morocco. In Proceedings of the Goldschmidt 2020, Honolulu, HI, USA, 21–26 June 2020. [[CrossRef](#)]
91. Valenza, K.; Moritz, R.; Mouttaqi, A.; Fontignie, D.; Sharp, Z. Vein and karst barite deposits in the western Jebilet of Morocco: Fluid inclusion and isotope (S, O, Sr) evidence for regional fluid mixing related to Central Atlantic rifting. *Econ. Geol.* **2000**, *95*, 587–606.
92. Burisch, M.; Walter, B.F.; Wälle, M.; Markl, G. Tracing fluid migration pathways in the root zone below unconformity-related hydrothermal veins: Insights from trace element systematics of individual fluid inclusions. *Chem. Geol.* **2016**, *429*, 44–50. [[CrossRef](#)]
93. Burisch, M.; Markl, G.; Gutzmer, J. Breakup with benefits -hydrothermal mineral systems related to the disintegration of a supercontinent. *Earth Planet. Sci. Lett.* **2022**, *580*, 117373. [[CrossRef](#)]
94. Laville, E.; Piqué, A. La distension crustale atlantique et atlasique au Maroc au début du Mésozoïque: Le rejeu des structures hercyniennes. *Bull. Société Geol. De Fr.* **1991**, *162*, 1161–1171.
95. Piqué, A.; Laville, E. L'ouverture de l'Atlantique Central: Un rejeu en extension des structures paléozoïques. *Comptes Rendus De L'Académie Des Sci. Paris* **1993**, *317*, 1325–1328.
96. Piqué, A.; Laville, E. The central Atlantic rifting: Reactivation of Palaeozoic structures. *J. Geodyn.* **1996**, *21*, 235–255. [[CrossRef](#)]
97. Essarraj, S.; Boiron, M.C.; Cathelineau, M.; Banks, D.A.; El Boukhari, A.; Chouhaïdi, M.Y. Brines related to Ag deposition in the Zgounder silver deposit (Anti-Atlas, Morocco). *Eur. J. Mineral.* **1998**, *10*, 1201–1214. [[CrossRef](#)]
98. Essarraj, S.; Boiron, M.C.; Cathelineau, M.; Banks, D.A.; Benharref, M. Penetration of surface evaporated brines into the Proterozoic basement and deposition of Co and Ag at Bou Azzer (Morocco): Evidence from fluid inclusions. *J. Afr. Earth Sci.* **2005**, *41*, 25–39. [[CrossRef](#)]

99. Essarraj, S.; Boiron, M.C.; Cathelineau, M.; Tarantola, A.; Leisen, M.; Boulvais, P.; Maacha, L. Basinal brines at the origin of the Imiter Ag-Hg deposit (Anti-Atlas, Morocco): Evidence from LA-ICP-MS data on fluid inclusions, halogen signatures and stable Isotopes (H, C, O). *Econ. Geol.* **2016**, *111*, 1753–1781. [[CrossRef](#)]
100. Essarraj, S.; Boiron, M.C.; Cathelineau, M.; Tarantola, A.; Leisen, M.; Boulvais, P. Basinal brines at the origin of the Imiter Ag-Hg deposit (Anti-Atlas-Morocco): Evidence from LA-ICP-MS data on fluid inclusions, Halogen signatures and stable isotopes (H, C, O). A reply. *Econ. Geol.* **2017**, *112*, 1273–1277. [[CrossRef](#)]
101. Walter, B.F.; Burisch, M.; Markl, G. Long-term chemical evolution and modification of continental basement brines—A field study from the Schwarzwald, SW Germany. *Geofluids* **2016**, *16*, 604–623. [[CrossRef](#)]
102. Haschke, S.; Gutzmer, J.; Wohlgemuth-Ueberwasser, C.; Kraemer, D.; Burisch, M. The Niederschlag fluorite-(barite) deposit, Erzgebirge/Germany—A fluid inclusion and trace element study. *Miner. Depos.* **2021**, *56*, 1071–1086. [[CrossRef](#)]
103. Guilcher, M.; Albert, R.; Gerdes, A.; Gutzmer, J.; Burisch, M. Timing of native metal-arsenide (Ag-Bi-Co-Ni-As±U) veins in continental rift zones—In situ U-Pb geochronology of carbonates from the Erzgebirge/Krušné Hory province. *Chem. Geol.* **2021**, *584*, 120476. [[CrossRef](#)]